Subject: Final Technical Report for AF STTR FA9550-04-C-0080
Covered Period: 09/01/2004 to 05/31/2005
Program Manager: Dr. Charles Y-C Lee

Summary of Phase I Accomplishments

The Phase I materials development effort was highly productive with the proposed Phase I milestones accomplished or exceeded. The results of Phase I have successfully demonstrated that an air-stable, high mobility n-type organic material can be synthesized and integrated into a process to form an organic CMOS process. Phase I has further demonstrated effective solutions to the challenges that are generally associated with such integration, including the development of an appropriate dielectric and electrode which are compatible with p-type materials as well. Major accomplishments were:

1. N-Type molecular semiconductors
   - Synthesized carbonyl-containing oligothiophenes
   - Fully characterized new compounds, films
   - TFT fabrication, evaluation, $\mu \sim 2$ cm^2/Vs (a record) and Ion:Ioff $\sim 10^9$

2. Solution-processable n-type semiconductors
   - Synthesized new polythiophenes
   - Fully characterized new materials
   - TFT fabrication, evaluation
   - Solution-processed n-type films fabricated, characterized
   - TFT fabrication, evaluation, $\mu \sim 0.06$ cm^2/Vs (a record) and Ion:Ioff $\sim 10^5$

3. Gate dielectrics
   - New nanoscopic dielectric materials
   - Low leakage currents ($< 10^{-8}$ A/cm^2), high breakdown fields (> 5 MV/cm), large gate capacitance --up to 2500 nF/cm^2 ; $k = 16$ ((a record).
   - Enabled organic CMOS technology at low voltages (< 2 V)

4. Transistor Characteristics
   - DFHCO-4T was used in several structures resulting in relatively high mobility. Mobility. Top contact devices with 1000A SiO$_2$dielectric resulted in 0.9 cm^2/Vs. When PEDOT electrodes are used, mobility was 0.18 cm^2/Vs, demonstrating the possibility of injecting electrons through a pn tunnel junction formed by the PEDOT and the accumulated electrons in the DHFCO-4T channel. When used in a bottom contact structure, mobility was 0.02 cm^2/Vs with Au source drain contacts that have been treated with SAMs to improve injection.

   - FTPCDI was used in a bottom contact, achieving a mobility of 0.017 cm^2/V-s.

20050622 109

- PDI-C8CN2 was used in a bottom contact transistor structure to achieve a mobility of 0.04 cm^2/Vs.

5. Injection Characteristics

- DFCO-4T was evaluated for injection characteristics in top contact devices with channel lengths in the range 50 µm to 1 mm. Observations confirmed that contact resistance effects do not substantially reduce the effective mobility at these channel lengths.

- Various fabrication methods using Au electrodes with channel lengths of 7.5 µm were explored, resulting in mobilities in the range 0.02-0.04 cm^2/V-s. Bottom contact devices with high mobility are generally more difficult to achieve due to the disordered region at the interface between the metal and semiconductor that impedes carrier transport. The best contacts were achieved with a combination of surface treatments.

- A new method of forming contacts to a n-channel OFET was developed, this one using injection of electrons though a p-n tunnel junction with a conductive polymer PEDOT as the source and drain contact. This approach yielded the highest mobility of any bottom contact n-channel OFET at 0.18 cm^2/Vs.

6. Circuits

- CMOS inverters with gain of 9 were produced.

- Ring oscillator frequencies of 2.5 kHz in vacuum with pentacene and DHFCO-4T with 7.5 µm channel length devices.

- Ring oscillator frequencies of 10 kHz in air with pentacene and PDI-C8CN2 with 7.5 mm channel length devices. We expect much higher frequencies in optimized low-capacitance structures which we are currently developing.

2

Table of Contents

In this final report, the work completed in Phase I is reported in detail. Specifically, this report covers the following:

1. Synthesis and characterization of molecular n-type semiconductors

1.1 Carbonyl-Functionalized Quaterthiophenes. In the previous report, we described the design rationale, synthesis, and characterization of quaterthiophenes containing the C=O group (**DHCO-4T, DFHCO-4T,** and **DFHCO-4TCO**) and compared their properties with those of the unfunctionalized (α4T) and C=O-free **DH-4T** and **DFH-4T** systems. We now report record mobilities for an –type conductor.

Top-contact FET devices were fabricated as described previously. Briefly, semiconductors **1 – 3** (~ 50 nm) were vapor-deposited on HMDS-treated p-doped Si with thermally grown oxide (300 nm
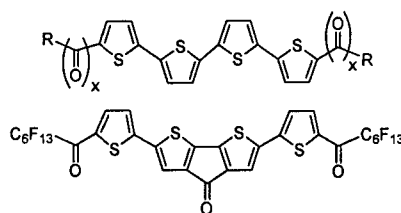
DHCO-4T (1) : x = 1, R = C_6H_{13}
DFHCO-4T (2) : x = 1, R = C_6F_{13}
DH-4T : x = 0, R = C_6H_{13}
DFH-4T : x = 0, R = C_6F_{13}
α4T : x = 0, R = H
DFHCO-4TCO (3)

SiO_2, C_i ~ 10 nF/cm^2) substrates maintained at temperatures (T_D) between 25 - 90 °C. OFET fabrication was completed by vapor-depositing source-drain Au contacts (~ 50 nm). Measurements were performed in air and vacuum (~ 10^{-5} Torr), and the standard saturation FET equation employed to calculate carrier mobilities. All of the new oligothiophenes exhibit *very high* electron mobilities (μ_e) in vacuum or inert atmosphere, with average values as a function of deposition temperature (T_D) shown in Figure 1.

Note that for some **DFHCO-4T** devices μ_e as high as ~ 0.6 cm^2 V^{-1}s^{-1} has been measured and recent results from our UT collaborators indicte that mobility close to 0.9 cm^2 V^{-1}s^{-1} can be achieved when contact resistance is taken into account. Interestingly, **DHCO-4T** films also exhibit relatively *large hole* mobilities (μ_h up to 0.01 cm^2 V^{-1}s^{-1} at T_D = 70°C) at all deposition temperatures. Ambipolar transport has been observed previously in blend/bilayers and single component
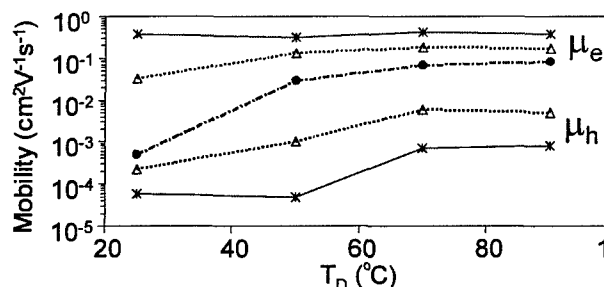
Figure 1. Electron (red) and hole (blue) mobilities vs. film deposition temperature (T_D) for DHCO-4T (Δ), DFHCO-4T (∗), and DFHCO-4TCO (•) in vacuum. μ_e for DFHCO-4T is after I_2 vapor treatment.

OFETs but with modest figures of merit, large μ_e and μ_h imbalances, and only for narrow T_D ranges. To our knowledge **DHCO-4T** is the first organic conductor exhibiting unoptimized μ_e/μ_h values as high as ~ 0.1/0.01 cm^2 V^{-1}s^{-1} (vacuum, T_D = 70-90 °C). **DFHCO-4T** also exhibits ambipolar behavior but only after I_2 vapor treatment. From the transfer plots, very high I_{on}:I_{off} ratios are observed for electrons, > 10^7. Maximum current gains for holes are > 10^8 for **DHCO-4T**. The sub-threshold swings (S), indicating how sharply the devices turn on, are in the 1.3-4.9 V/decade range and turn-on voltages |V_0| are ~ 5-30 V. Importantly, more electron-deficient **DFHCO-4T** and **DFHCO-4TCO** also operate well in air with μ_e's ~ 5/10x lower in magnitude.

Considering the important results shown above, we optimized the mobility of the best candidate (**DFHCO-4T**) via treatment of the dielectric surfaceWhen the SiO$_2$ dielectric surface is covered with a thin layer (~ 20 nm) of polystyrene (**PS**), the electron mobility is greatly
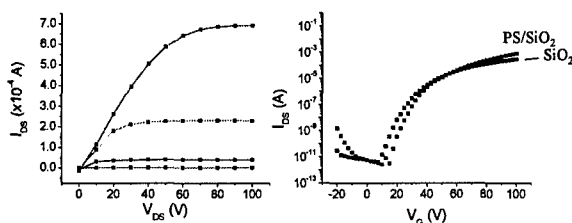
Figure 2. Output (left) and transfer (right) plots for DFHCO-4T-based devices.

4

enhanced. Figure 2 shows the FET output and transfer plots for **DFHCO-4T**-based TFT devices using PS-SiO$_2$ vs. SiO$_2$. Exceptionally high carrier mobilities of ~ 1.9 cm^2/Vs (versus ~ 0.4 cm^2/Vs for the control) and I$_{on}$:I$_{off}$ ratios of ~ 10^9 have been obtained. These results demonstrate that our n-type semiconductors in combination with the proper dielectric have great potential. Furthermore, note that this material was deposited at room temperature and further optimization of the film growth process should further enhance these mobilities. Finally, we have been synthesizing an even more electron depleted thiophene core **DFHCO-4TCO2**, which should be completely air stable thiophene-basad n-type semiconductors. The final synthetic step is in progress.
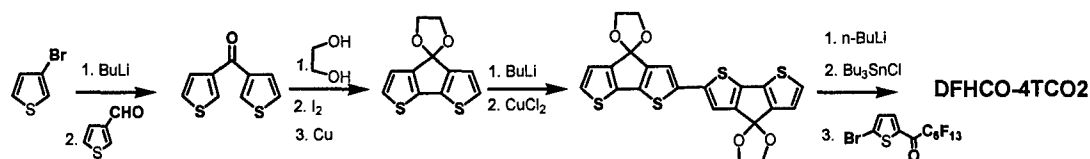
1.2. Perfluoroarene-carbonyl derivatives. Studies in our group previously demonstrated that fluorinated substitutents on oligothiophenes can switch conduction from p- to n-type on OFETs. As shown in the previous section, carbonyl substitution further increases this effect, giving OFETs with an electron mobility ~ 2 cm^2 V^{-1} s^{-1}. It is also known that phenyl ring incorporation can enhance cofacial crystal packing, which can favorably effect the transfer integral for electron hopping between adjacent molecules and facilitate crystallization. Hence, a new series (**DPCO-4T** and **DFCO-4T**) of acyl-quaterthiophenes was synthesized to take advantage of these three phenomena. The fluorine-free compound (**DPCO-4T**) was synthesized to have a better picture of the substitution effects. The synthesis of the new compounds is described in Scheme 1. Introduction of the carbonyl functionality was achieved via Friedel-Crafts acylation of 2-bromothiophene with the proper benzoyl chloride. These molecules were coupled to bis(tributyltin)bithiophene via the Stille reaction to give the semiconductors **DPCO-4T** and **DFCO-4T**. These compounds are gradient sublimed twice before device fabrication.
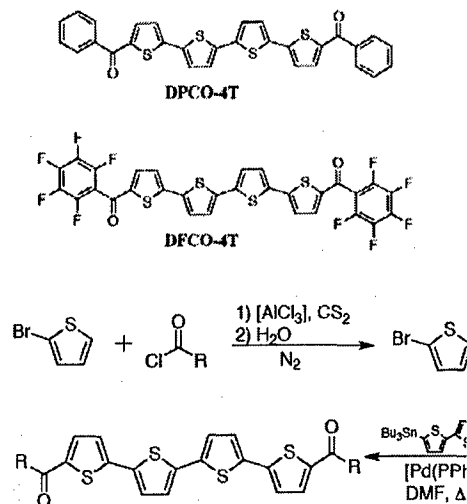
Scheme 1.

Conventional analytical techniques were used to characterize the semiconductors and intermediates.
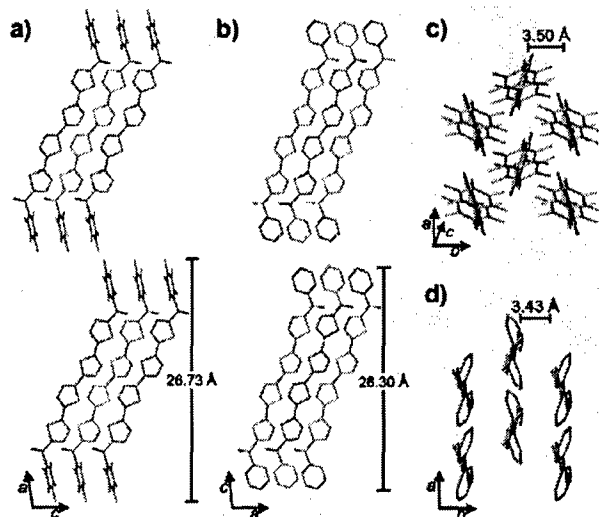
Figure 3. Crystal structure of **DFCO-4T** (a) and **DPCO-4T** (b) viewed perpendicular to the long axis of the unit cell (hydrogen atoms not shown). Note the remarkably similar herringbone packing in **DFCO-4T** (c) and **DPCO-4T** (d), respectively, viewed along the long crystallographic axis.

Table 1. Charge carrier mobilities (μ, cm^{2}V^{-1}s^{-1}) and current on/off ratios ($I_{on}:I_{off}$) for top contact OFETs fabricated with **DFCO-4T** and **DPCO-4T**.

| Deposition Method	T_D [a] (°C)	DFCO-4T		DPCO-4T	
		μ_e	$I_{on}:I_{off}$	μ_h	$I_{on}:I_{off}$
Vapor	25	0.02	10^4	0.012	10^5
Vapor	50	0.17	10^5	0.014	10^5
Vapor	70	0.31	10^5	0.028	10^5
Vapor	80	0.39	10^7	-	-
Vapor	90	0.17	10^7	0.043	10^5
Drop Cast [b]	110	0.011	10^4	8×10^{-4}	10^3
Drop Cast [b]	120	0.15	10^6	-	-

[a] Substrate deposition temperature. [b] From xylene.

Electrochemistry reveals two single electron reductions at –1.0 V and –1.1 V vs. SCE in THF for **DFCO-4T**. Additionally single crystals were obtained and their crystal structures determined using x-ray diffraction (Figure 3). The dihedral angle between the phenyl ring and thiophene core was found to be 45.8° for **DPCO-4T** and 53.0° for **DFCO-4T**. The intermolecular stacking distance (defined as the distance between the center of two adjacent quaterthiophene cores – 4.62 Å for **DPCO-4T** and 4.82 Å for **DFCO-4T**) is similar for both compounds. The difference in parameters can be attributed to the greater van der Waals radus of fluorine vs. that of hydrogen.

Field effect transistors with vapor deposited semiconductor were fabricated with Au top-contact electrodes as previously reported.[4] Films (50 nm) were deposited onto temperature controlled HMDS treated SiO$_2$/n$^+$-Si substrates by vapor deposition (10^{-6} Torr) and by drop casting. A 50 nm layer of Au was then deposited through a shadow mask to define the source and drain electrodes. OFET characterization was preformed in a high vacuum probe station that was back-filled with Argon. High electron mobilities (μ_e) of ~0.4 cm^{2}V^{-1}s^{-1} are observed for vapor deposited **DFCO-4T** films (T_D = 80 °C) with a threshold voltage (V_T) of ~30 V. This μ_e value is one of the highest reported and is very reproducible from sample to sample – reflecting the favorable crystal packing affinity of this molecule. In solution cast devices, μ_e is exceptionally high with a maximum of ~0.2 cm^{2}V^{-1}s^{-1} ($I_{on}:I_{off}$ = 10^6; V_T = 50 – 70 V). To our knowledge, this is the *highest OFET electron mobility* for a solution-cast molecular semiconductor reported to date. The non-fluorinated material, **DPCO-4T**, exhibits hole mobilities (μ_h) in vapor deposited films up to ~0.04 cm^{2}V^{-1}s^{-1} ($I_{on}:I_{off}$ = 10^5; V_T ~-20 V), but no electron conduction has been observed. Films of this material drop-cast from xylenes have μ_h of 3×10^{-4} cm^{2}V^{-1}s^{-1}. Similar dependencies of mobility on T_D are observed in both vapor deposited semiconductors, with the highest mobilities near a T_D of 80 °C - 90 °C (Table 1). This trend is consistent with the increased crystallinity observed by TF-XRD with increasing T_D.

Cyclic voltammetry of the above semiconductors in THF reveals two reversible single electron reductions (E_1/E_2 (V) vs. S.C.E.) at -1.05/-1.16 in **DFCO-4T** and at -0.95/-1.30 in **2**. Irreversible oxidative features are observed at +1.07/+1.22 in **DFCO-4T**. UV-vis data (**DFCO-4T** λ_{max} = 456 nm; **DPCO-4T** λ_{max} = 444 nm, Fig. S5) indicates that the HOMO-LUMO optical band gap (E_g) is 2.40 eV for **DFCO-4T** and 2.46 eV for **DPCO-4T**. The orbital energies (E_{HOMO}/E_{LUMO} (eV)) are -6.19/-3.79 for **DFCO-4T** and -6.35/-3.89 for **DPCO-4T**. Surprisingly, E_{LUMO} of the n-type **1** is slightly less negative (0.1 V) than that of p-type **DPCO-4T**. Based upon conventional understanding, electron affinity (E_{LUMO}) and ionization potential (E_{HOMO}) are primary factors in determination of charge carrier type – therefore, it is surprising that **DFCO-4T** exhibits electron mobility in the solid-state, while **DPCO-4T** primary conducts holes. An explanation may lie in subtle molecular conformation differences in the crystal structures. In the solid-state, the dihedral angle between the electron-withdrawing carbonyl groups and the thiophene core is much greater in **DPCO-4T** than in **DFCO-4T**. This is probably a result of crystal packing forces as the DFT-derived vacuum geometry indicates that the carbonyl lies in the thiophene plane for both molecules. This greater conjugation in **DFCO-4T** should enhance

6

resonance stabilization of the negatively charged core in the solid-state. Since such packing effects are not present in solution, the geometry and hence the electronic structure/energetics are more similar – in agreement with MO computations and electrochemical experiments.

1.3. Cyanated perylene and naphthalene derivatives. Previously we reported the synthesis of two new *core-cyanated* perylene-3,4:9,10-bis(dicarboximide) (PDI) derivatives, **PDI-CN₂** and **PDI-FCN₂**, which exhibit the highest air-stable n-type OFET carrier mobilities reported to date (Table 2), in combination with low threshold voltages and substantial processing versatility.

PDI-CN₂ : R =

PDI-FCN₂ : R = *n*-CH₂C₃F₇
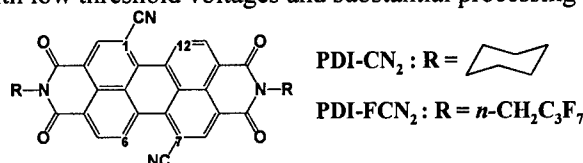
The new compounds were synthesized using modifications of literature core cyanation and *N*-fluoroalkylation procedures, and were characterized by heteronuclear NMR, mass spectrometry, optical absorption spectroscopy, photoluminescence, cyclic voltammetry, thermogravimetric analysis, and single-crystal x-ray diffraction. **PDI-CN₂** exhibits excellent air-stability and solubility in organic solvents, while reduced pressure TGA scans indicate only slight (~2%) decomposition during sublimation (see report 2). The low energy LUMO indicated by the first reduction potential, -0.07 V vs. S.C.E., suggests improved n-type charge carrier stability versus alkyl-substituted PDI cores (~ -0.4 V vs. S.C.E.). Moreover, the results with **PDI-CN₂**-derived OFETs (see below) motivated the synthesis of a new PDI derivative with additional electron-withdrawing substituents and greater volatility, hence **PDI-FCN₂**. The electrochemical and optical data of **PDI-CN₂** (Table 1) reveal further depression of the LUMO level vs. **PDI-CN₂**, while TGA indicates quantitative sublimation.

**Table 2.** Electronic and OFET characteristics of cyanated perylene diimide derivatives.

Compound	λ_{abs} (nm)[a]	λ_{em} (nm)[a]	$E_{(1)}$ (V)[b]	$E_{(2)}$ (V)[b]	μ (cm² V⁻¹ s⁻¹)	I_{on}/I_{off}
PDI-CN₂	530	547	-0.07	-0.40	0.10	10⁵
PDI-FCN₂	530	545	+0.04	-0.31	0.64	10⁴

[a] measured in THF (10⁻⁵/10⁻⁶ M), [b] measured in 0.1 M TBAPF₆ solution in THF vs. S.C.E.

In an attempt to increase n-type activity of imide-substituted arenes even further, the synthesis of a core-cyanated naphthalene semiconductors was pursued. The first target was *N,N'*-bis(n-octyl)-2,6-dicyanonapthalene-1,4:5,8-tetracarboxylicdiimide (**NDI-8CN₂**), which was synthesized according to Scheme 1. **NDI-8CN₂** was characterized with cyclic voltammetry, UV-visible spectroscopy, and photoluminescence. The electrochemistry in dichloromethane reveals a first reduction potential of -0.06 V vs. S.C.E. and a
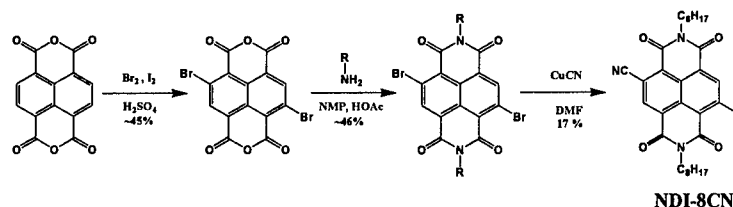
Scheme 2

second reduction potential of – 0.67 V vs. S.C.E.; approximately 0.4 V easier to reduce than uncyanated naphthalene diimide. UV-vis data reveals minimal shifts in the absorption spectrum from unsubstituted naphthalene diimide with absorption maxima at 376 nm, and 361 nm. Interestingly, absorption spectra in DMF reveal a population of **NDI-8CN₂** in its reduced radical anion state, as well as the neutral species, a consequence of reduction by the small dimethylamine impurity in DMF. This observation demonstrates the remarkable electron accepting capabilities of **NDI-8CN₂**, even in the presence of ambient O₂. Photoluminescence spectroscopy reveals

7

emission maxima of 452 nm, 533 nm, and 569 nm. Presently, the broad emission responsible for the 533 nm and 569 nm peaks is attributed to an eximer-like state and the emission at 452 nm is thought to be the monomeric species. Studies are currently ongoing to understand this phenomenon. The absolute molecular orbital energies can be estimated at LUMO = -4.3 eV and HOMO = -7.3 eV, based on the reduction potential and optical bandgap. Interestingly, the wide band gap of almost 3.0 eV makes this material optically transparent.

FET characterizations are underay. Vapor-deposited OFETs in the top-contact configuration were fabricated in the following manner. Films of **NDI-8CN$_2$** ~ 50 nm thick were vapor deposited (0.2 Å s^{-1}, P ~ 10^{-6} Torr) onto a n$^+$-doped Si (100) wafer with a 300 nm thermally grown SiO$_2$ dielectric. Gold electrodes 50 nm thick were thermally evaporated onto the thin films through a shadow mask. The silicon substrates were cleaned for 5 minutes with an O$_2$ plasma and were used immediately afterwards (SiO$_2$) or further treated with either 1,1,1,3,3,3-hexamethyldisilazane vapor (HMDS), octadecyltrichlorosilane (OTS), or 1H,1H,2H,2H-perfluorooctyltrichlorosilane(FOS) prior to film deposition. The substrates were maintained at 90 °C during film deposition. Under these conditions, the mobility of **NDI-8CN$_2$** approaches 0.05 cm^{2}V^{-1}s^{-1}, I$_{on}$/I$_{off}$ ~ 10^5, and V$_{TH}$ ~ 5 V. These parameters exhibit minimal variation when tested under vacuum and ambient atmosphere. Detailed information is summarized in Table 3.
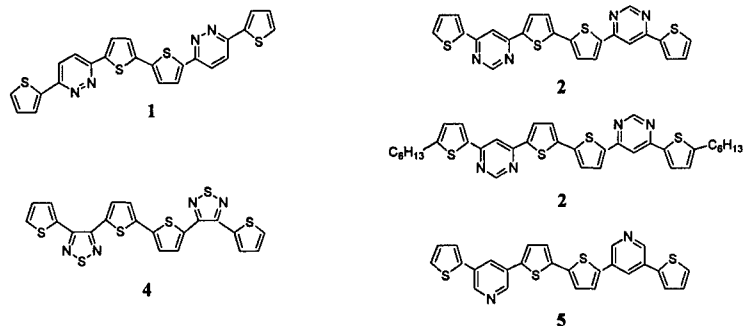
Table 3. OFET characteristics of cyanated perylene diimide derivatives.

Substrate treatment	SiO$_2$ μ^{vac} (cm^{2}V^{-1}s^{-1})	I$_{on}$/I$_{off}^{vac}$	V$_{TH}^{vac}$ (V)	μ^{air} (cm^{2}V^{-1}s^{-1})	I$_{on}$/I$_{off}^{air}$	V$_{TH}^{air}$ (V)
none	4x10^{-2}	10^4	-3	4x10^{-2}	10^5	+4
HMDS	3x10^{-2}	10^5	-1	2x10^{-2}	10^5	+11
OTS	3x10^{-2}	10^5	+8	4x10^{-2}	10^5	+6
FOS	1x10^{-3}	10^3	-10	4x10^{-4}	10^1	-20

With the exception of the FOS-treated substrate, **NDI-8CN$_2$** is relatively insensitive to typical substrate conditions. While the mobilities are modest in this early study, we are optimistic that these can be improved since we have observed mobilities of ~0.3 cm^{2}V^{-1}s^{-1} with similar uncyanted naphthalene diimides (not shown). Importantly, we can routinely achieve I$_{on}$/I$_{off}$ of ~ 10^5 in the preliminary studies on this compound, compared to ~10^4 for the optimized cyanated perylene diimides. We are currently investigating the reason for this difference to understand and improve this figure of merit. Finally, the improved V$_{TH}$ of ~ 0 V for **NDI-8CN$_2$** (vs. ~ 20 V for uncyanated naphthalene diimide based semiconductors) will make these materials more suitable for use in a variety of applications.

1.4. Electron-poor heterocycle-thiophene derivatives. An alternative approach to n-type conductors would be to employ electron-poor heterocycle rings (pyridine, pyrimidine, pyridazine, thiadiazine rings) into the π core structure rather than strong electron-withdrawing core substituents (Figure 4). We initiated and achieved in the syntheses of mixed azine-thiophene oligomers shown below. Systems **1 – 3** were synthesized by Stille

Figure 4. Structure of azine-containing oligothiophenes.

palladium-catalyzed reactions in good yields (Scheme 3) and purified by either sublimation or recrystallization.

8
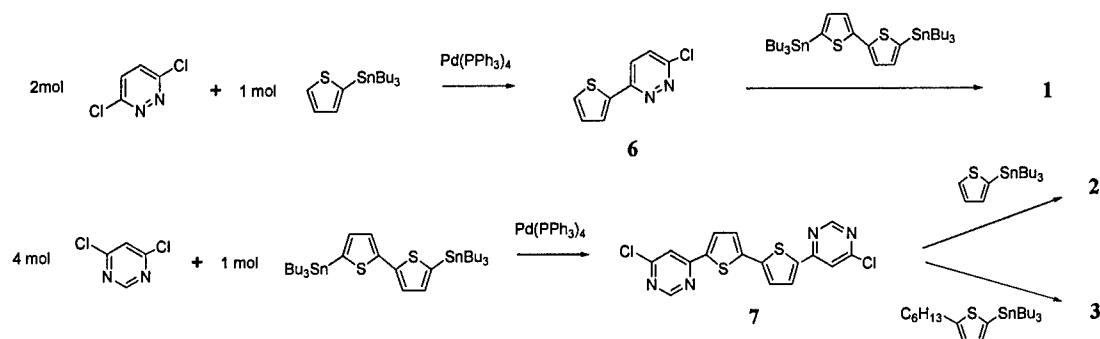
Scheme 3

Molecular characterization as well as film deposition and TFT measurements are in progress.

2. Synthesis and characterization of polymeric n-type semiconductors

A second goal of Phase I is to initiate the synthesis of polymeric n-type semiconductors, which would depend strongly on the properties found for the related molecular semiconductors. We envisioned a number of possible structures formally derived form the best molecular semiconductors we discovered (**DFHCO-4T, PDI-CN$_2$, DFCO-4T**). All of these polymers have the common feature of being functionalized with electron-withdrawing groups to lower the LUMO levels and stabilize the injected electrons. We have now achieved their syntheses.

2.1. Perfluoroalkyl-, perfluoroary-, and perfluoroalkylcarbonyl-substituted polythiophenes. The synthetic goal is to develop efficient routes to new regioregular n-type conducting polymers. Among the structures in this family we proposed, the initial efforts were devoted to the synthesis of polymers **P1**, **P2**, and **P3**. The first two polymers are essentially polythiophenes containing different ratios of the perfluorohexyl substituent, whereas the third is a thiophene/perluorophenyl copolymer. The common characteristic of these new polymeric systems is the presence of strong electron-withdrawing groups which should decrease LUMO energies allowing for easy electron injection. Key building blocks for polymer preparation are monomers **M1**, **M2**, and **M3** (Scheme 4).
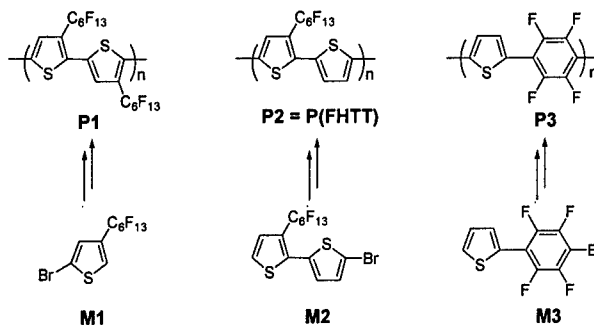
Scheme 4

All of the new polymer precursors have been obtained in good yields according to Scheme 5. Once the monomer precursors have been obtained, there are several approaches for preparing the corresponding polymers. We initially employed the McCullough (Ni-catalyzed coupling of Grignard reagents) and Rieke (Ni/Pd-catalyzed coupling of Zn derivatives) methods (Scheme 6).

McCullough (i) 1. LDA; 2. MgBr$_2$; 3. NiCl$_2$(dppp)

Rieke (ii) 1. LDA; 2. ZnCl2

Scheme 5

9
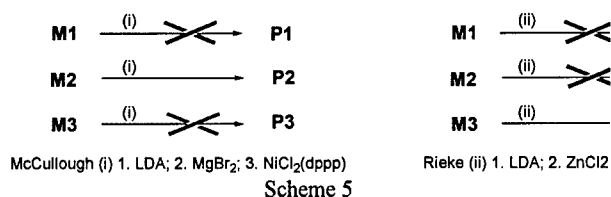
Following these routes, monomer **M1** doesn't afford the corresponding polymer. On the other hand, **M2** and **M3** give polymers **P2** [**P(FHTT)**] and **P3**, respectively, in good yields (> 70%). Polymer **P3** is insoluble in common organic solvents. **P2** has been extensively characterized by elemental analysis,

Br
1) BuLi, -78°C
2) TMSCl
Br
1) Cu bronze, 120°C
2) C₆F₁₃I
C_6F_{13}
CF₃SO₃H
C_6F_{13}
Br₂
AcOH, 90 °C

Br
BrMg
PdCl₂(dppf)
Br
S
$C_6F_{13}I$
Cu
C_6F_{13}
NBS
M2

F F
Br
F F
SnBu₃
Pd(PPh₃)₄
M3

Scheme 6

molecular weight determination (GPC, Mn = 5-7K, PDI = 1.1-1.15, 25-30 thiophene units), DSC (214°C, LC transition; 258°C, melting point), optical absorption (408 nm, THF; 445 nm, film) and emission (581 nm, THF; 588, film), ^{1}H and ^{19}F NMR. Characterization of redox properties through cyclic voltrammetry reveals that the fluorinated polymer has lower reduction potentials than the corresponding alkyl-substituted polymer [**P(HTT)**] (synthesis and full characterization not shown), which should make the system behave more *n*-type (Table 4). Furthermore, characterization of thermal properties via differential scanning calorimetry shows that the fluorinated polymer is thermally more stable and does not decompose until relatively high temperatures.

C_6H_{13}
P(HTT)

C_6F_{13}
P(FHTT)
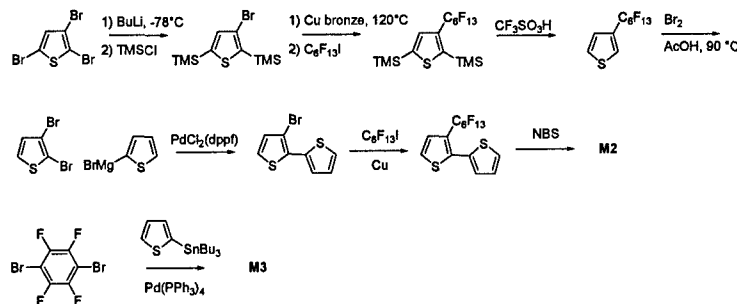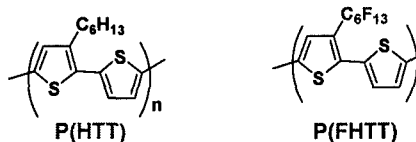
Figure 15 Molecular structures of the fully characterized polymers.

Table 4 Electrochemical redox potential data				
	Oxidation		Reduction	
P(HTT), THF	0.86	1.12	-1.71	————
P(FHTT), THF	————	————	-1.29	-1.64
P(HTT), Film	1.01	1.87	-1.76	————
P(FHTT), Film	1.89	————	-1.20	-1.49

Considering the satisfactory analytical data and the good solubility in aromatic solvents, **P(FHTT)** TFT devices were fabricated by casting from xylene at ~ 110 °C on Si-SiO₂ gate-insulator substrates. The films are smooth and shiny and exhibit an n-type channel mobility of ~ 10^{-6} with $I_{on}:I_{off}$ ratio of ~ 10^2 (Figure 6). Film and device optimization are in progress. Within this family, we also initiated the synthesis of regioregular poly 3-perfluorohexylcarbonylthiophene **P4**. The synthesis of the key monomer
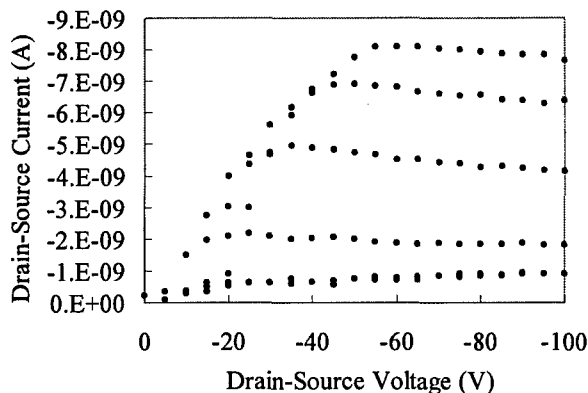
Figure 6. Output plot of a P(FHTT)-based TFT.

Drain-Source Current (A) vs Drain-Source Voltage (V)

10

precursor **M4** was successful (Scheme 4). Polymerization reactions are in progress.
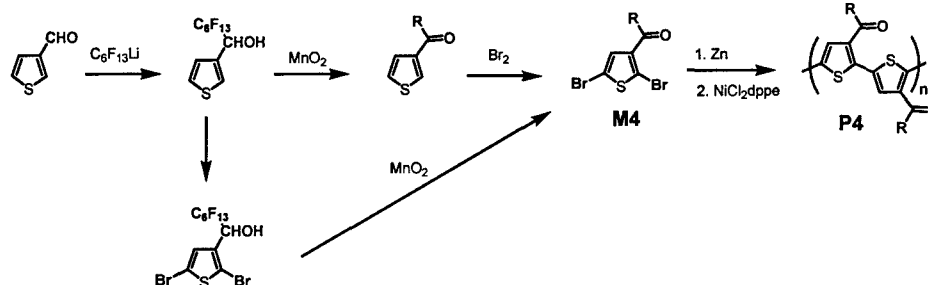
Scheme 6

Finally, we demonstrated that **DFCO-4T** has a very high intrinsic electron mobility of 0.4 cm² V⁻¹ s⁻¹ for vapor deposited films and 0.04 cm² V⁻¹ s⁻¹ for solution cast films (see Section 1.2). This is strong evidence that incorporation of a similar molecular structure into a polymer will likely yield a highly electron-conducting polymer. Using **DFCO-4T** as the repeat unit in the polymer, solublizing side chains are added to enhance solution processability, giving structure **P(COFCO-4T)**. Introduction of the carbonyl functionality was achieved via lithiation of 1,2,4,5-tetrafluorobenzene and subsequent reaction with thiophene-2-carbaldehyde to give the diol **7**. This molecule is then brominated to give **8** (not shown), then oxidized to yield **9**. The bithiophene core 4,4'-dioctyl-2,2'-dithiophene (**10**) was prepared via oxidative copper coupling and stannylated from the lithium salt as for unsubstituted bithiophene (Scheme 7). The Stille coupling was chosen because its established use 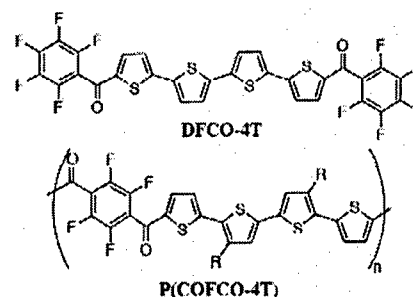in thiophene polymerizations and functional group compatibility. The two monomers **9** and **11** were dissolved in DMF and heated for several days in the presence of a tetrakis(triphenylphosphine)palladium(0) catalyst (Scheme 2).
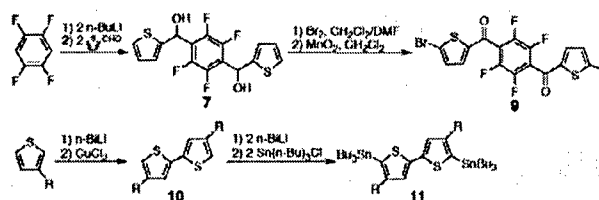
DFCO-4T

P(COFCO-4T)

Scheme 7

Conventional analytical techniques were used to characterize the semiconductors and intermediates. Films of **P(COFCO-4T)** were deposited by spin-casting and drop-casting from chloroform, thiophene, and 1,2,4-trichlorobenzene (TCB) solutions at concentrations of 1000 ppm and 10000 ppm. Drop and spun cast films from thiophene and chloroform exhibited uniform coverage and consistent color. The FET activity was tested using a standard device configuration with no current modulation observed. Bottom and top contact devices were fabricated and tested. The molecule **DFCO-4T** (similar to the monomer unit of the polymer) was dissolved with the polymer in hot xylenes at a concentration of 2500 ppm **P(COFCO-4T)** / 10000 ppm **DFCO-4T**. This solution produced films with significant crystallization by spin and drop casting, when diluted by a factor of 2 the films were more uniform and one device exhibited n-type current modulation (I_{on}/I_{off} = 10, V_t = 150 V, μ = 10⁻⁸ cm² V⁻¹ s⁻¹). However, we found that the polymer **P(COFCO-4T)** has good solubility in common solvents and forms high-quality films when spun cast from thiophene, xylenes, and trichlorobenzene. **P(COFCO-4T)** undergoes a reversible two
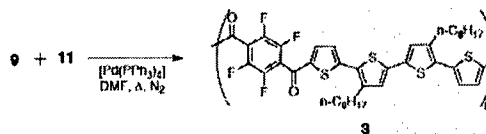
Scheme 8

electron reduction at -1.23 V plus an additional irreversible reduction at -1.60 V and three single electron oxidations at +0.96/+1.13 (reversible) and +1.40 V. E_g is 2.37 eV (λ_{max} = 455 nm) with the orbital energies (E_{HOMO}/E_{LUMO} (eV)) at -5.98/-3.61. An initial drop casting study was performed using blends of **DFCO-4T** and **P(COFCO-4T)** to take advantage of the high μ_e of the molecular semiconductor and the enhanced viscosity/ processability of the polymer. yielding μ_e ~10^{-3} cm^{2}V^{-1}s^{-1} ($I_{on}:I_{off}$ = 3 x 10^2 ; V_T ~53 V).

   2.2 Poly(N-alkylimido)thiophenes. The dicarboximide functionality is a strong electron-withdrawing functionality and is known to stabilize injected electrons. Indeed, some of the best air-stable n-channel semiconductors for OFET devices developed in our laboratory have been fabricated using dicarboximide-containing small molecules such as **PDI-CN₂** and **NDI-8CN₂**. From these reasons, polymers bearing a 3,4-dicarboximide-thiophene functionality were synthesized (Figure 7). Theoretical modeling indicates that **PCxI** has a slightly twisted structures with a dihedral angle ~ 20° between two adjacent thiophene rings, which is still sufficient for efficient intramolecular orbital overlap, while **PCxIT** and **PCxITT** are predicted to be planar. The synthesis of six polymers **PCxI**, **PCxIT**, and **PCxITT** (x = 8, 12) has been achieved. Purification of **PC8I** and **PC12I** was accomplished via soxlet extraction and solubilization/reprecipitation, and

R = n-octyl, x = 8
R = n-docecyl, x = 12

Figure 7. Structures of n-type polymers.

microanalytical data are satisfactory. The purification of the other four polymers and the synthesis of **PBCxIT**, **PBCxITT**, and **P6** are underway. **PC8I** and **PC12I** are homopolymers whereas all of the other compounds are co-polymers. The solubility of **PC8I**, **Pc8IT**, and **PC8ITT** in common organic solvents such as chloroform and xylene is low and a C12 alkyl tail is necessary to render **PcxI** soluble. All the polymers are fairly soluble in warm 1,2,4-trichlorobenzene. Optimization of film deposition conditions for FET fabrication is in progress.

3. Ultra-thin dielectric materials for low voltage operation

   3.1. Layer-by-layer molecular nanodielectrics. Typical "top-contact" OTFTs contain a semiconductor layer on top of a dielectric, together with an underlying gate electrode and top charge-injecting/extracting source and drain electrodes. Current flowing between source and drain electrodes (I_{DS}) on application of a drain-source bias (V_{DS}) is minimal when zero voltage is applied between gate and drain electrodes (V_G = 0) -- the device is "off". However, as V_G is increased in magnitude, charge carriers are accumulated at the semiconductor-dielectric interface, resulting in a gate-modulated I_{DS} ("on" state). Parameters characterizing TFT performance include the field-effect mobility (μ) and the current on/off ratio ($I_{on}:I_{off}$), defining the drain-source current ratio between "on" and "off" states. I_{DS} in the linear regime is then expressed by Eq. 1, where W and L are the TFT channel width and length, respectively, V_T the threshold voltage, and C_i the dielectric capacitance per unit area (Eq. 2 where k is the dielectric constant, ε_0 is the vacuum permittivity, and d is the dielectric thickness). Note that for a given device geometry and semiconductor, equivalent $I_{on}:I_{off}$ are achieved at lower operating biases by increasing C_i which

stabilizes the carrier density in the semiconductor channel. This is important for OTFTs considering the modest μ values of organic semiconductors--typically < 1 cm^{2}V^{-1}s^{-1} vs. 10^3 cm^{2}V^{-1}s^{-1} for crystalline Si. Furthermore, high-quality ultrathin gate dielectrics will be essential in combination with small channel lengths for high frequency operation and self-assembled molecular electronics.

$$I_{DS} = \frac{W}{L} \mu C_i \left[V_G - V_T - \frac{V_{DS}}{2}\right] V_{DS} \quad (1) \qquad C_i = \varepsilon_0 \frac{k}{d} \quad (2)$$

Recent efforts to increase C_i have striven either to increase k or to reduce d while managing the aforementioned challenges, using either self-assembled monolayers (SAMs) of simple monofunctional hydrocarbon chains or relatively thick sputtered films of conventional metal oxides having greater k than SiO$_2$, e.g., BaSr$_x$Ti$_{1-x}$O$_3$, Ta$_2$O$_5$, or TiO$_2$. As dielectrics, the high defect densities and fragility of monolayers results on low device yields and modest OTFT response. The approach reported here utilizes 3-D crosslinked dielectric multilayers grown from solution via self-limiting sequential deposition of the following σ-π building blocks (Fig. 8): (a) α,ω-difunctionalized hydrocarbon chains (**Alk** = **1**) which transversely crosslink, enabling precision stepwise layer build-up, increasing interchain packing, and reducing defects/pinholes. (b) Highly polarizable "push-pull" stilbazolium layers (**Stb** = **2**) self-assembled into oriented π-electron layers which should stabilize charge carriers in the semiconducting channel, including bound and free charges. (c) Octachlorotrisiloxane capping layers (**Cap** = **3**) which enhance multilayer structural robustness by capping/planarizing with a crosslinked, glassy siloxane polymer. The resulting OTFTs function in the sub-1V bias regime and exhibit very low leakage currents over large gate electrode areas, very large breakdown fields, and excellent device characteristics.

Figure 8. Schematic representation of the components of an organic thin-film transistor (OTFT) showing the molecular structures of various organic semiconductors (left) and self-assembled nanodielectrics I-III (right). Highly n-type doped Si(100) wafers with a 1.5 nm native oxide or smooth ITO (tin-doped indium oxide, a transparent conductor) were used as substrate/gate electrodes. Nanodielectric layers are then sequentially deposited from solutions of silane precursors **Alk**, **Stb**, or **Cap**. The OTFT device is completed by vacuum-deposition of 50 nm thick layers of p- or n-type organic semiconductors **1-4** or solution-deposition of semiconductor **5**, followed by source-drain gold electrode (100 nm) vacuum deposition.

To validate the modularity of this approach and to elucidate structure-function relationships, three nanodielectrics of incrementally varied structure and thickness were fabricated (Fig. 8). These are identified by the nomenclature: **I** (layers: **Alk+Cap**), **II** (layers: **Stb+Cap**), and **III** (layers: **Alk+Cap+Stb+Cap**). The microstructures, electrical properties, and responses of TFTs fabricated with **I** – **III** were characterized as reported below. The synchrotron X-ray reflectivity-derived thicknesses of the nanoscopic dielectrics are: 2.3 (**I**), 3.2 (**II**), 5.5 (**III**)

13

nm (± 10%). Optical absorption and optical second-harmonic generation measurements on **II** and **III** demonstrate net polar alignment of the **Stb** dipoles with an average molecular tilt angle of ~40° from the surface normal, while AFM and SEM images of **I** – **III** are featureless, with rms roughness ~ that of the Si substrate, 0.5-1.0 nm, and consistent with crack/pinhole-free morphologies. The excellent insulating properties of **I** – **III** are demonstrated by cyclic voltammetry (Fig. 9a) using ferrocene probe solutions with either bare ITO-coated glass working electrodes (ITO = tin-doped indium oxide) or those coated with **I** – **III**. From the magnitude of the current at any potential, it can be seen that there is passivation of the ITO surface with respect to ferrocene oxidation/reduction as successive ultra-thin dielectric layers are built up, arguing that these multilayers eliminate the majority of pinholes (potential short circuits) which would compromise OTFT performance. This conclusion is further confirmed by quantitative solid-state leakage current measurements through the nanodielectrics, made on metal-insulator-semiconductor (MIS) and metal-insulator-metal (ITO-based MIM, see Supplementary Information) sandwich structures fabricated by thermal evaporation of 200 × 200 μm^2 Au contacts onto **I** – **III** (Fig. 9b). While Si/Si native oxide substrates exhibit very large current densities of ~ 0.1 – 1.0 A/cm^2 at 1.0 V, thin films of **I**, **II**, and **III** reduce the leakage currents by ~ 6 and ~ 9 orders of magnitude, respectively. Current densities for **III** (~ 10^{-9} A/cm^2) can be compared to reported SAM values spanning the broad range 10^{-5}- 10^{-9} A/cm^2 for smaller area (100 × 100 μm^2) Al contacts to 10^{0}-10^{-5} A/cm^2 reported by others. The measured breakdown fields for **I-III** (5-7 $MVcm^{-1}$) rival or exceed those reported for far thicker (~ 50 nm) metal oxide and polymer dielectric layers (0.1-5 $MVcm^{-1}$), previously employed in OTFTs.
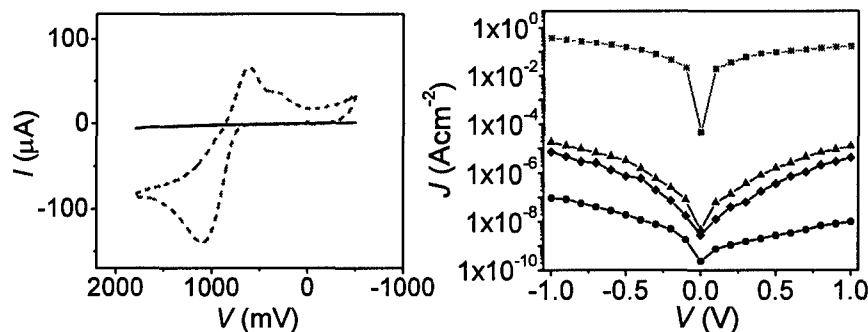
Figure 9. Leakage current measurement for nanodielectrics I-III. **a**, Film pinhole assay by cylic voltammetry (current vs. voltage) using ferrocene/ferrocenium$^+$ solutions in THF/tetrabutylammonium perchlorate (Ag pseudo-reference electrode; Pt counter electrode) using bare ITO (dotted line) and nanodielectrics I – III coated ITO as working electrodes (solid line). Electrode areas ~ 0.5 cm^2. **b**, Measured leakage current density J versus voltage plots without (bare substrate) and with nanodielectrics I – III in metal-insulator-semiconductor (MIS) sandwich structures on n$^+$-Si. As expected, the J-V curves are slightly asymmetric around 0.0 V, reflecting the different nature of the Au-siloxane-insulator and n$^+$-Si-native oxide-insulator interfaces.

Capacitance-voltage (C-V) measurements were carried out on MIS structures at 10^2 – 10^5 Hz (Fig. 10). With n$^+$-Si as the semiconductor, capacitance is expected (and found) to increase on sweeping the bias with respect to the metal contact from negative (depletion in the semiconductor) to positive (accumulation). Capacitance- and dielectric loss (tanδ)-frequency plots (Fig. 4b) reveal maximum capacitances C_i = 400 (**I**); 710 (**II**); 390 (**III**) $nFcm^{-2}$ (± 5%) at 10^2 Hz, with slight fall-off (~ 15%) at higher frequencies. These values are far greater than the capacitance of conventional 300 nm-thick SiO_2 dielectrics typically used for OTFTs (~ 10 $nFcm^{-2}$), greater than our estimates for the best siloxane SAM (~140 $nFcm^{-2}$), and comparable to the highest reported for a metal oxide dielectric, C_i = 150-750 $nFcm^{-2}$ in far thicker (d = 50-100 nm) sputtered TiO_2 films. The nanodielectric loss factor (~10^{-1}-10^{-2}) is greater than in optimized CMOS SiO_2 dielectrics (~ 10^{-4}) and, at all frequencies, **I** – **III** exhibit 0.1-0.4 V hystereses.

14

Annealing at 120-180 °C reduces all hystereses to < 0.1V and reduces frequency-dependent C-V dispersion, suggesting that pristine I-III contain some quantities of fixed positive charges (Q_f), ~ 2-5×10^{12} cm^{-2} (24,25). Interface state densities (D_{it}) calculated from standard C-V and G-V (conductance-voltage) plots are ~ 3×10^{12} eV^{-1} cm^{-2}. Importantly, annealing reduces Q_f and D_{it} to ~ 10^{11} cm^{-2} and ~10^{11} eV^{-1} cm^{-2}, respectively -- near standard values for SiO$_2$ and many high-k dielectrics.
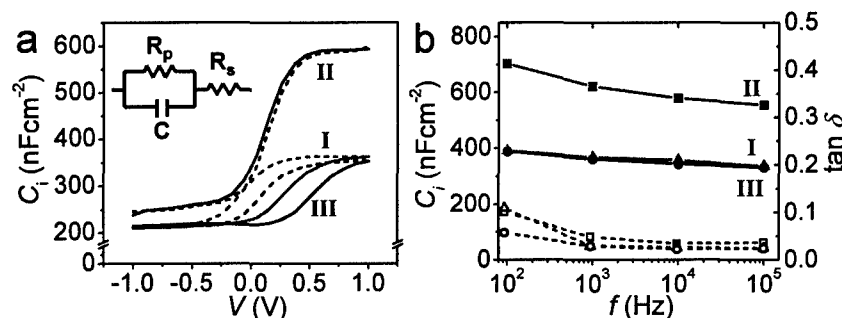
Figure 10. Capacitance/loss measurements for I-III in metal-insulator-semiconductor structures. **a,** Measurement of nanodielectric capacitance-voltage electrical characteristics for structures I (red), II (blue), and III (black) of Fig. 1 at 10^4 Hz (solid line is the forward scan, broken line is the return scan). (**Inset**): equivalent circuit representation. Note that the contribution of the nanodielectric capacitor (C) component to the total circuit impedance predominates over the series (R_s) and parallel (R_p) resistances as well as over the estimated parasitic capacitance. **b,** Frequency (f) dependence of the maximum capacitance and dielectric loss in the accumulation regime (1 V) between 10^2 – 10^5 Hz for the indicated nanodielectrics.

Also important are the magnitudes of the effective dielectric constants $[k_{eff} = (C_i \cdot d_{\text{I-III}})/\varepsilon_0$, Eq. 2] achieved in I-III which are best estimated from measuring C_i in MIM structures. In fact, the presence of the Si-SiO$_2$ interface strongly limits the maximum charge storage in the accumulation layer resulting in underestimated C_i values. If the contributions of individual **Alk** and **Stb** organic layers (k_{org}) are estimated by pragmatically assuming parallel-plate capacitors in series of thickness $d_{\text{I-III}} = d_{org} + d_{cap}$ (Eq. 3) with **Cap** forming a SiO$_x$ network (d_{cap} = 0.83 ± 0.1 nm by XRR), then k_{eff} of **I** and **II** can be approximated by multilayers composed of **Alk** and **Stb** monolayers and oxide layer (k_{ox} ~ 3.9).

$$\frac{d_{tot}}{k_{eff}} = \frac{d_{org}}{k_{org}} + \frac{d_{cap}}{k_{cap}} \tag{3}$$

From the maximum MIM capacitance values [C_i = 1100 (**I**); 2500 (**II**); 760 (**III**) nFcm^{-2} (± 5%)], k_{org} of the **Alk** and **Stb** layers is estimated to be ~2.5 (close to that of bulk paraffin and alkyl SAM) and ~16, respectively. This result illustrates the strategic importance for this and future work of highly π-polarizable dipolar layers in enhancing k_{eff}, hence increasing C_i while preserving excellent insulator properties.

OTFTs (Fig. 8; L = 100 μm, W = 5 mm) were next fabricated on I-III, with all devices exhibiting reproducible I-V characteristics at low biases with classical linear and saturation response, as exemplified with typical p- (**1**) and n-type (**3**) semiconductors (Fig. 5). Note that the operation window can be enlarged substantially by substituting multilayer **III** for **II/I** (Fig. 5b), due to the increased breakdown resistance, in agreement with the aforementioned leakage current data. Similar transistor characteristics are obtained for a range of vapour/solution-deposited organic semiconductors, demonstrating broad generality. In marked contrast, control devices fabricated with a thicker SiO$_2$ dielectric require far larger operating voltages for useful I_{DS} (Fig. 11, inset). Nanodielectric **III** was next evaluated extensively in TFT geometries. Typical laboratory scale device fabrication yields were >98%. Table 5 summarizes data for

15

semiconductors **1-5** (operating biases 0.0 - ±1.0 V) and for comparison, those using standard 300 nm SiO_2 as the gate dielectric (operating biases 0 - ±100 V). Note that comparable μs are now obtained at far smaller operating biases, and that V_Ts are now only fractions of volts. The I_{on}:I_{off} ratios should be further enhanced with second-generation device configurations and by more elaborate patterning of the semiconducor. Note also that TFTs fabricated on glass-coated ITO gates function comparably, demonstrating that a Si/Si native oxide gate is not required to achieve excellent performance (Figs. 11, 12) and that optically transparent low-voltage devices are readily fabricated. These nanodielectrics can also be used to fabricate flexible TFTs on commercially-available plastic (Mylar)-coated ITO gates (Fig. 13), demonstrating applicability to transparent flexible plastic electronics. Finally, note that the thermal stability of the new nanodielectrics (T_{dec} > 200-300 °C) suggests compatibility with inorganic semiconductors that can be deposited at low temperatures.

Table 5 Field Effect Transistor Data (operating biases 0.0 - ±1.0 V) for Organic Semiconductors 1 – 5 using the Nanodielectric III on n+-Si substrates.[a]

| Semiconductor	μ ($cm^2V^{-1}s^{-1}$)	I_{on}:I_{off} [b]	V_T (V)
	0.06 (0.04)	7×10^2 (10^4)	0.08 (-4)
1	0.03 [c]	6×10^{2} [c]	0.05 [c]
	0.02 [d]	1×10^{3} [d]	0.06 [d]
	0.04 [e]	8×10^{2} [e]	0.03 [e]
2	0.002 (0.02)	5×10^2 (10^4)	-0.17 (2)
3	0.02 (0.2)	6×10^2 (10^5)	0.21 (14)
4	0.003 (0.001)	3×10^2 (10^4)	-0.22 (20)
5	0.01 (0.02)	2×10^2 (10^4)	-0.20 (-40)

[a] Data in parentheses are for 300 nm thick SiO_2 dielectric devices. All TFT mobilities (μ_{FET}) and threshold voltages (V_T) are calculated in the saturation regime (*11*). [b] Calculated at V_G = 0.0 - ±1.0 V (0 - ±100 V) and V_{DS} = ±1.0 V (±100 V). [c] Data for nanodielectric **III** on glass-ITO substrates. [d] Data for nanodielectric **II**. [e] Data for nanodielectric **I**.
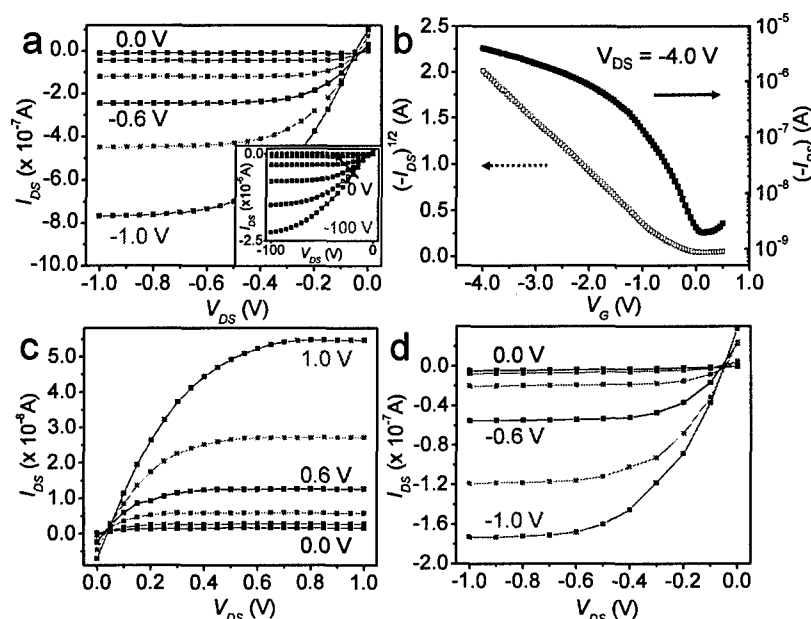

Figure 11. Current-voltage performance characteristics as a function of gate voltage (V_G; values indicated in vertical sequence in each plot) for nanodielectric-based organic transistor devices fabricated with the indicated organic semiconductors (molecular structure key in Fig. 8) on an n^+-Si gate: **a**, **II**/semiconductor **1**; p-type. (Inset)

SiO$_2$(300nm)/semiconductor 1; p-type. b, TFT transfer plot of current vs. gate voltage for III/semiconductor 1; p-type. c, III/ semiconductor 4; n-type d, OTFT fabricated on a transparent conducting ITO gate: III/ semiconductor 1; p-type.
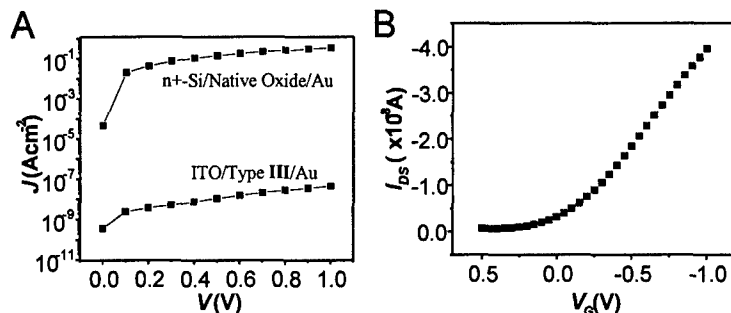
Figure 12. (A) Current density versus voltage plots for n$^+$-Si-native oxide and ITO-type III –Au structures. (B) Transfer plot for **1** on ITO-type III-based OTFT device.
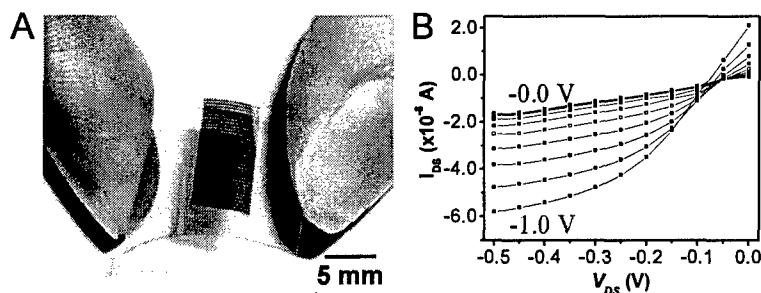

Figure 13. (A) Picture of flexible ITO-based TFT. Note that the roughness of this ITO is (B) TFT output characteristics for semiconductor **1** as a function of V_G using nanodielectric-based type **III** grown on Mylar-ITO substrates.

These results demonstrate that designed self-assembling building blocks incorporating extensive 3-D crosslinking and π-electron constituents enable precise, solution phase fabrication of extremely thin, nanostructurally ordered, pinhole-free, high-capacitance/high-k/low leakage organic multilayer dielectrics. These molecule-derived dielectrics (2.3-5.5 nm) can be efficiently integrated into large-area p- and n-channel OTFTs (single TFT area ~10^{12} nm^2) demonstrating great uniformity with a variety of substrates. The results argue that many of the charge transporting limitations of current organic semiconductors can be circumvented and that this assembly methodology combined with crosslinkable high-k π-electron modules should be adaptable to creating even higher dielectric constant and higher capacitance multilayers.

3.2. Ultra-thin polymeric dielectrics. It is known that OTFTs are limited by high operating voltages, typically $\gg$ 10 V, due to the intrinsic low carrier mobilities of the semiconductors and the low capacitances of the gate dielectrics (typically thick SiO$_2$ or polymer films). As we discussed in the previous section, a possible solution is to employ moderate-high capacitance self-assembled nanoscopic organic multilayers. However, the gate insulator materials exhibiting greatest potential for OTFTs are polymers due to their ready integration into a printing process. Thus, PVP, PMMA, and polyimides have been investigated as gate insulators with a limited number of organic semiconductors, however the resulting OTFTs operate at relatively high voltages. This reflects the substantial insulator thicknesses (usually $\gg$ 0.3 μm) required to reduce gate leakage currents to acceptable levels, thereby affording low capacitance metrics (typically $\ll$ 20 nF cm^{-2}). An innovative alternative recently reported by Bao, *et al.* grows polymeric insulators *in situ* on the gate surface, and offers, in principle, tunable thickness control. However, reported capacitances are again modest ($\sim$ 3 nF cm^{-2}) for low-voltage OTFT applications.

17

Recently, the Cambridge group described the thinnest polymer dielectrics achieved to date (50-100 nm) for top-gate polymer-based OTFTs, which operate at relatively low voltages (~ 10 V) with a triarylamine semiconductor. This represents a significant advance, however the polymerization/annealing temperatures are quite high (230-290 °C) and reported device I-V saturation characteristics not ideal. In this report, we demonstrate a new low temperature approach which realizes high-quality crosslinked OTFT polymer dielectrics from straightforward polymer/molecular precursors. The crosslinking chemistry ensures that subsequent device layers can be spin-coated or printed on top without dissolution of the dielectric and that the dielectric is covalently bonded to the surface of typical gate materials. To our knowledge, these 10-20 nm-thick polymeric insulators exhibit the largest capacitances and lowest leakage currents (considering the thickness range) achieved to date for conventional and crosslinked polymer gate OTFTs, as well as afford devices with extremely low operating biases. Moreover, we show here that this approach is applicable to diverse gate and semiconductor materials.

The new crosslinked polymer blend (CPB) materials (Fig. 2) are prepared by spin-coating of a solution of an appropriate polymer and α,ω-bis(trichlorosilyl) crosslinking reagent using procedures described in Methods, resulting in films with 10-20 nm thicknesses as established by profilometry. All operations are performed in air in a simple fume hood. The films are next cured at ~ 100 °C for times dependent on the spin-coating solvent (e.g., 5-10 min for THF). The chlorosilane hydrolysis/condensation/crosslinking process occurs within seconds in ambient. Note that we have not attempted to fully optimize processing at this stage. Films of greater thicknesses if required (vide infra), can be obtained simply by multiple spin-on depositions since the CPB material is insoluble in the mother solutions at all stage of curing. To assess the influence of CPB structure (Fig. 14) and the effects of polymer microstructure and crosslinker on film properties, two polymers, poly-4-vinylphenol (PVP) and polystyrene (PS), and three crosslinkers, hexachlorodisiloxane (C_0), 1,6-bis(trichlorosilyl)hexane (C_6), and 1,12-bis(trichlorosilyl)dodecane (C_{12}), were investigated. The crosslinked films, CPVP-C_n and CPS-C_n, are structurally quite different. In CPVP-C_n, PVP chains are σ-bonded to a siloxane network whereas for CPS-C_n, PS chains are simply embedded as guests in a crosslinked matrix. It will be seen that this affords materials with substantially different properties versus those of neat PVP and PS films of similar/greater thicknesses, and which were characterized by atomic force microscopy (AFM) as well as metal-insulator-metal (MIM) and metal-insulator-semiconductor (MIS) leakage and capacitance measurements. Table 6 collects important metrics for these materials.


Crosslinked Polymer Blend (CPB) Dielectrics
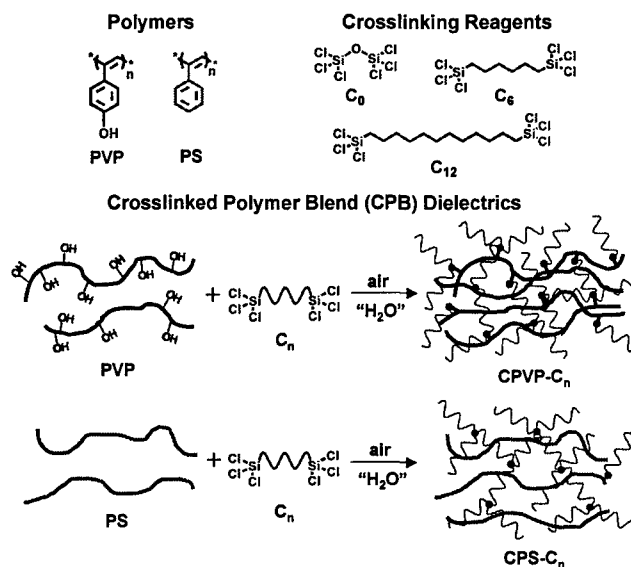
Figure 14. Chemical structures of the polymer and siloxane crosslinkers employed and the CPB dielectric fabrication process.

Table 6. Summary of dielectric (10 kHz) and film properties of polymeric dielectrics.

Dielectric	Film Thickness[a] (nm)	RMS Roughness[a] (nm)	C_i[b] (nF cm^{-2})	ε[c]
CPVP-C$_0$	18	6-8	305	6.2
CPVP-C$_6$	18	2	300	6.1
CPVP-C$_{12}$	20	6	289	6.5
CPS-C$_0$	12	8-10	220	3.0
CPS-C$_6$	10	1.5	218	2.5
CPS-C$_{12}$	13	5	200	2.9
PVP	133	6	42	6.4
PS	122	2	19	2.6
SiO$_2$[d]	300	2	11	3.9[e]

[a] Measured on Si substrates (substrate rms roughness ~ 0.5 nm). [b] Measured on MIS structure. [c] Calculated from Eq. 2.[d] From commercial source. [e] Literature value.

AFM images of CPB films reveal that surface morphology is more dependent on crosslinking reagent than on polymer architecture. Since a smooth dielectric-semiconductor interface is essential for efficient transport in the TFT channel, AFM data provide important information for initial materials evaluation. The **CPVP-C$_0$** and **CPS-C$_0$** AFM images exhibit very rough surfaces, having large densities of grains and flakes, with a 6-10 nm rms roughness. In contrast, CPB films crosslinked with **C$_6$** are far smoother, exhibiting a rms roughness of ~ 1.5-2 nm, and exhibit no major defects or pinholes. Note that thin/thick neat **PVP** and **PS** films are also very smooth. However, close examination reveals that smooth regions are accompanied by major pinholes which will inevitably compromise dielectric performance. The **CPS-C$_{12}$** films are
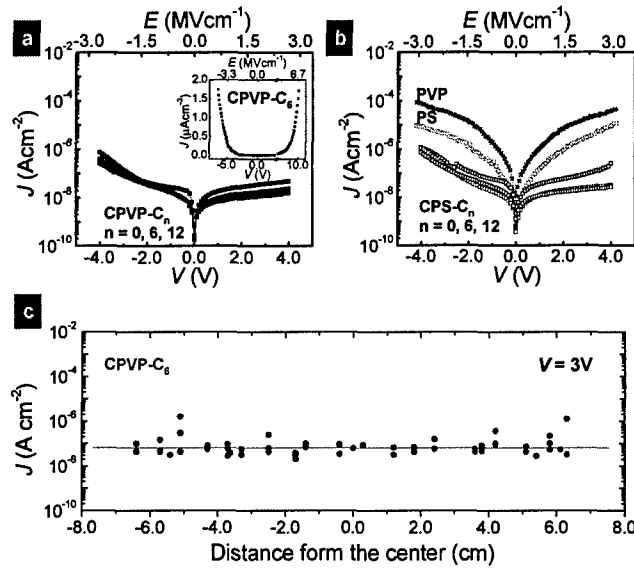
Figure 15. Electrical properties of **CPVP-** (filled symbols) and **CPS-** (empty symbols) C$_n$ (C$_0$ = black, C$_6$ = red, C$_{12}$ = blue) films versus those of neat **PVP** (green filled symbol)/**PS** (green empty symbol) films. Note that the voltage axis refers to CPB films only. **a.** Leakage current density J vs. voltage plots for **CPVP-C$_n$** [d (nm) = 17 (C$_0$), 14 (C$_6$), 10 (C$_{12}$)] films. **Inset:** Extended plot for a **CPVP-C$_6$** film (13 nm). **b.** Leakage current density J versus voltage plots for **CPS-C$_n$** [d (nm) = 12 (C$_0$), 11 (C$_6$), 13 (C$_{12}$)], **PVP** (133 nm), and **PS** (122 nm) films. **c.** Leakage current density J distribution (V = 3 V) for a **CPVP-C$_6$** film (~ 24 nm) over a 130 mm Si wafer.

19

Somehow rougher than **CPVP-C$_6$** and **CPS-**, possibly because the longer **C$_{12}$** chains aggregate in the spin-coating solvents, resulting in grainy crosslinked films. The greater **CPVP-C$_0$** and **CPS-C$_0$** film roughness is probably the combined result of greater **C$_0$** moisture sensitivity, versus α,ω-alkane-linked chlorosilanes (**C$_6$** and **C$_{12}$**), resulting in rapid crosslinking as well as absence of a "flexible" linker between the silyl termini, yielding a less flexible siloxane network. Note that **CPVP-C$_6$** and **CPS-C$_6$** also planarize rough substrates such as commercial kitchen Al foil or glass. For example, the rms roughness of commercial Al substrates, $\sim$ 11-14 nm, is reduced to $\sim$ 4-6 nm after depositing a $\sim$ 60 nm-thick **CPVP-C$_6$** film.

The dielectric characteristics of the crosslinked dielectric films were next evaluated via quantitative leakage current and capacitance measurements. Fig. 15 shows typical current density-electric field (*J-E*) plots for MIS structures fabricated with CPB and **PVP/PS** insulators, demonstrating that these ultra-thin crosslinked materials exhibit superior insulating properties vs. the corresponding neat polymers of far greater thickness. Leakage current densities for d = 10-20 nm **CPVP-C$_n$** and **CPS-C$_n$** films are $10^{-7} - 10^{-8}$ A cm^{-2} up to $E \sim 2$ MV cm^{-1} ($\pm$ 3V) compared to $10^{-4} - 10^{-7}$ A cm^{-2} (E $\sim$ 2 MV cm^{-1}) for d = 120-130 nm **PVP** and **PS** films. The former metrics are also substantially lower than those of a several hundred nm-thick melamine-crosslinked **PVP** films and comparable to those of μm-thick polymer dielectrics and far thicker oxide films. Furthermore, Fig. 15 demonstrates that CPB films of excellent electrical uniformity can be deposited by the present procedure over a 13 cm diameter Si wafer, with average leakage current densities for a **CPVP-C$_6$** film ($\sim$ 24 nm) of 9.8 $\pm$ 2.3 x 10^{-8} A cm^{-2} (V = 3 V) when sampling 60 wafer locations. Furthermore **CPVP-C$_n$** films strongly adhere to substrates, do not undergo delamination/cracking on substrate bending or solvent treatment (e.g., 30 s sonication in organic solvents) in accord with the highly crosslinked/bonded microstructure. Leakage currents, capacitances, and OTFT characteristics (vide infra) are invariant to solvent exposure, demonstrating potential for subsequent solution-phase processing/fabrication steps. In contrast, partial delamination or complete dissolution occurs for **CPS-C$_n$** and **PVP** or **PS** films, respectively.

Despite excellent adhesion and solvent resistance, **CPVP-C$_n$** films can be conveniently patterned as required for via formation using conventional lithography and reactive ion etching (RIE) or buffer oxide etching (BOE). As proof-of-concept, Fig. 17a shows an image of shadow-mask fabricated Au pads on a **CPVP-C$_6$**/Si substrate. After dielectric removal from the exposed areas (Fig 17b), the resulting patterned MIS structures exhibit leakage current densities comparable to those of unpatterned areas (Fig. 17b), demonstrating that RIE/BOE patterning does not alter the quality of the underlying dielectric layer. After Au removal, the optical image clearly shows the patterned dielectric region, while profilometry and AFM (Fig 17c) demonstrate that the thickness of the dielectric is unchanged. Finally, Au pad deposition in regions where the dielectric layer was removed demonstrate formation of excellent electrical contacts to the bottom (gate) with J increased > 6 orders of magnitude versus those in MIS structures (Fig. 18b).

To quantify CPB film capacitances, dielectric constants, and loss factors as a function of frequency ($10^3 - 10^6$ Hz), capacitance-voltage (C_i-V) and capacitance-frequency (C_i-f) measurements were performed on MIS (M = Au, S = n+-Si) and MIM (M = ITO, Au) structures. Both structures provide quantitatively similar results. Representative C_i-f plots are shown in Fig. 18, with the data (Table 6) demonstrating that CPB films exhibit large capacitances [C_i (**CPVP-C$_n$**) $\sim$ 300 nFcm^{-2}, C_i (**CPS-C$_n$**) $\sim$ 225 nFcm^{-2}; $\pm$ 5% at 10^3 Hz], far greater than typical OTFT 300 nm-thick SiO$_2$ gate dielectrics ($\sim$ 10 nFcm^{-2}). In contrast, the capacitance of thin **PVP** and **PS** films (< 20 nm, not shown) cannot be measured due to large leakage currents, and the capacitances of $\sim$ 130 nm-thick films (still too leaky for practical OTFTs; Fig. 17b) are substantially lower (Table 1). Note that CPB C_i values are reproducible and stable with time, indicating in contrast to PVP, CPB polymers are minimally hygroscopic. Samples do not exhibit appreciable variation in C_i/J characteristics over 17 months, and dielectric strength is recovered after breakdown. Breakdown fields are between 3-6 MVcm^{-1} (see inset Fig. 16a for **CPVP-C$_6$**)

20

depending on CPB structure and voltage scan direction. The formal dielectric constants calculated using Eq 2, are 6.1-6.5 and 2.5-2.9 (10 kHz) for **CPVP-C$_n$** and **CPS-C$_n$** films, respectively. These values are reasonable considering that the reported **PVP** and **PS** dielectric constants are ~ 3.6[48]-8 and ~ 2.5, respectively - - close to values independently measured in this study (6.4 and 2.6, respectively).
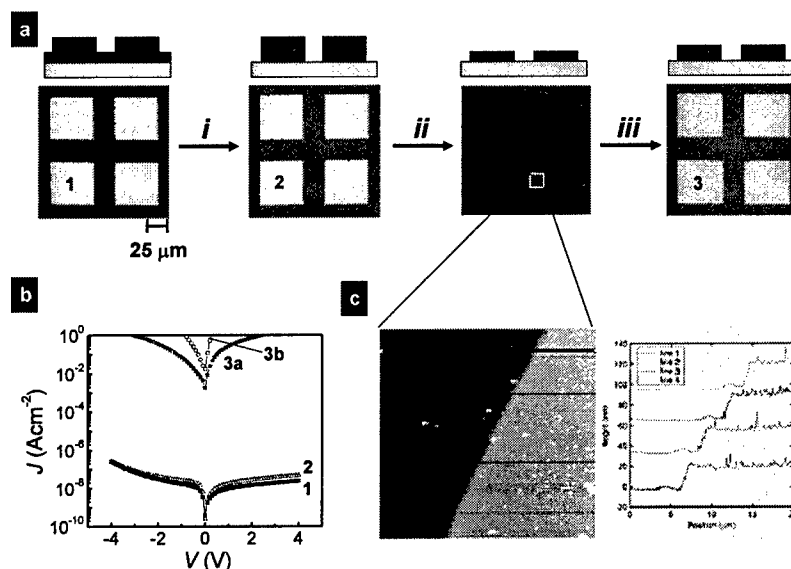
Figure 16. Patterning of **CPVP-C$_6$** films and corresponding film electrical properties. **a.** Optical micrographs of a series of pads having the structure depicted above the corresponding image [gray = Si substrate; blue = dielectric (23 nm); orange = Au (50 nm)]. Patterning process: i) Dielectric etching with RIE (5 min) or BOE (30 s); ii) Au etching with I$_2$-KI-H$_2$O (1 min); iii) RIE or BOE, and then Au deposition. **b.** Leakage current density recorded on the unpatterned (line 1) and patterned (line 2) dielectric on Si and after dielectric removal with RIE (line 3a) and BOE (line 3b). **c.** AFM line scans of the dielectric step after patterning.
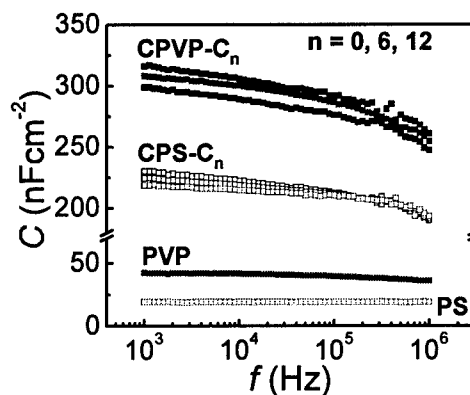
Figure 17. Capacitance-frequency plots (1 – 1000 kHz; film thicknesses given in Table 1) for the polymer dielectrics investigated in this study.

The loss factors for the present dielectrics are also reasonably low (< 0.1 at 10^4 Hz) considering that processing is not yet fully optimized. Finally, all of the CPB films exhibit little hysteresis in the C_i-V plots, suggesting that the positive fixed charge density is very low. Typical hysteresis shifts are < 0.1 V and < 0.5 V for **CPVP-C$_n$** and **CPS-C$_n$**, respectively, and do not vary with air exposure. Exhaustive polymer purification, design/blending of different (co)polymers, and film fabrication in a dust-free environment should further enhance performance. Furthermore,

21

dielectric constant tuning should be possible with crosslinker optimization. From the above data, **CPVP-C$_6$** is the most attractive member of the CPB series in terms of large capacitance, low leakage currents, and smooth morphology, and so **CPVP-C$_6$** was examined most extensively for OTFT fabrication and evaluation.

The principal TFT structures investigated utilized **CPVP-C$_6$** and, for comparison, **CPS-C$_6$**, spin-coated on the gate, followed by semiconductor and Au source-drain contact deposition (top-contact TFT). Devices fabricated on n$^+$-Si substrates were used to demonstrate CPB compatibility with a variety of semiconductors, whereas pentacene OTFTs were investigated to demonstrate CPB compatibility with many gate materials in both top- and bottom-contact geometries. For semiconductor generality, a variety of molecular and polymeric p- (hole transporter) and n- (electron-transporter) channel semiconductors were selected, with films deposited by either vapour- or solution methods. Fig. 18 shows typical *I-V* plots for pentacene (vapor-deposited, p-type) and **CuFPc** (vapor-deposited, n-type). These data demonstrate that **CPVP-C$_6$**-based TFTs exhibit excellent linear/saturation characteristics and operate at low voltages (as low as < 1 V), reflecting the large capacitance and low leakage currents of the CPB gate dielectric. Typical laboratory-scale device yields approach 100%. In marked contrast, control devices fabricated with a thicker (300 nm) SiO$_2$ dielectric film require far larger operating voltages for a useful I_{DS}. CPB OTFT data summarized in Table 7 show that carrier mobilities are comparable to those of SiO$_2$-based devices fabricated under identical conditions. Moreover, the V_Ts are now only a fraction/few volts and subthreshold voltage swing (S) parameters are very low. Note that for ease of initial comparison, all semiconductor films discussed here were deposited at an identical substrate temperature (60 °C), not necessarily optimum for each semiconductor.

Table 7. Field effect transistor data for CPVP- and CPS-C$_6$ –based devices with different organic semiconductors and gate substrates.^{a}

| Semicond.	Dielec. /Subst.	μ (cm^{2}V^{-1}s^{-1})	I_{on}:I_{off}^{b}	V_T^{d} (V)	S^{e} (V/dec.)
1. Pentacene	CPVP-C$_6$ / n$^+$-Si	0.1 (0.3)	10^4 (10^5)	-1.8 (-2.3)	0.45 (8)
2. DH-6T	CPVP-C$_6$ / n$^+$-Si	0.1 (0.1)	10^3 (10^4)	0.9 (-4)	0.47
3. DHPTTP	CPVP-C$_6$ / n$^+$-Si	0.01 (0.02)	10^4 (10^5)	-1.2 (-5)	0.28
4. P3HT	CPVP-C$_6$ / n$^+$-Si	4x10^{-3} (5x10^{-3})	10^2 (10^3)	1.2 (20)	0.54 (9)
5. CuFPc	CPVP-C$_6$ / n$^+$-Si	5x10^{-3} (3x10^{-3})	10^3 (10^4)	0.5 (20)	0.40
6. Pentacene^c	CPVP-C$_6$ / n$^+$-Si	2x10^{-3}	10^3	-0.7 ^{c}	0.63 ^{c}
7. Pentacene	CPS-C$_6$ / n$^+$-Si	0.08	10^4	-2.0	0.35
8. Pentacene	CPVP-C$_6$ / ITO-Glass	0.01	10^3	-0.4	0.58
9. Pentacene	CPVP-C$_6$ / ITO-Mylar	0.06	10^4	-0.6	0.29
10. Pentacene	CPVP-C$_6$ / Al	0.03	10^3	-0.2	0.28

^{a} Data in parentheses are for 300 nm-thick SiO$_2$ devices with the semiconductor films grown under the same condition as for **CPVP-** and **CPS-C$_6$**. All TFT mobilities (μ) and threshold voltages (V_T) are calculated in the saturation regime. ^{b} Calculated at V_G = 0.0 - ±4.0 V (0 - ±100 V) and V_{DS} = ±4.0 V (±100 V). ^{c} Data for bottom-contact configuration. ^{d} Threshold voltage. ^{e} Subthreshold voltage swing (S = dV_G / d(log I_{DS})).

Pentacene/**CPVP-C$_6$** OTFT devices achieve μ ~ 0.1 cm^2 V^{-1}s^{-1} versus ~ 0.3 cm^2 V^{-1}s^{-1} for those with SiO$_2$ dielectrics and I$_{on}$/I$_{off}$ ~ 10^4 at V$_G$ = 4 V. Bottom-contact pentacene TFTs also perform well (Table 7, entry 6). Also, typical n-type semiconductors such as **CuFPc** behave similarly on **CPVP-C$_6$** vs. SiO$_2$ dielectrics with μ ~ 0.005 cm^2 V^{-1}s^{-1} and I$_{on}$/I$_{off}$ > 10^3 (Table 7, entry 5). Note that these TFTs show little hysteresis [(ΔI_{DS}/I_{DS})$_{max}$ < 10 %)] in I_{DS}-V_{DS} plots, confirming the good quality of the dielectric material (Inset Fig. 18b). Importantly, solution depositing an additional organic layer on top does not adversely affect CPB insulator properties. Thus, TFTs fabricated with **P3HT** (spin-coated from CHCl$_3$) and **DHPTTP** (solution-cast from xylene) display good transistor response characteristics at very low voltages (entries 2, 3). Pentacene TFTs having a **CPVP-C$_6$** gate dielectric were also fabricated on a variety of substrates,

demonstrating broad versatility. Thus, TFTs on ITO/glass (entry 8), ITO/Mylar (entry 9), and kitchen Al foil (entry 10) exhibit excellent response characteristics, and the Al foil-based devices can be repeatedly bent with negligible degradation of TFT performance (Figs. 19a and b). Note that these results are achieved on large device areas, and more sophisticated patterning and structure optimization should additionally improve performance. Finally, the remarkable stability of OTFTs fabricated with CPB gate dielectrics (when the semiconductor is itself environmentally stable) is shown in Fig. 19c Pentacene TFTs can be continuously cycled in air (relative humidity ~ 80 %, T = 22-25 °C) between V_G = 0 and + 3 V without detectable "on" current and I_{on}/I_{off} degradation over periods > 60 h. This result confirms that the dielectric-semiconductor interface is largely free of reactive groups that can act as charge carrier traps.
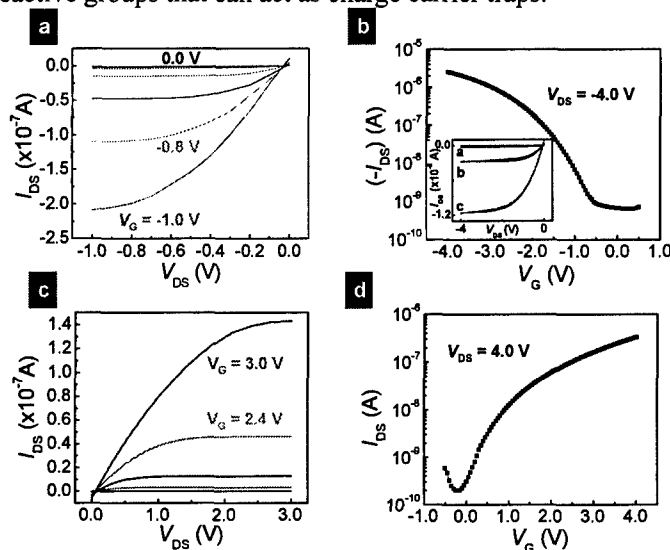
Figure 18. Performance of representative TFT devices at low biases with a crosslinked **CPVP-C$_6$** gate dielectric layer on an n$^+$-Si gate. **a.** Current-voltage plot as a function of V_G for DH-6T (p-type). **b.** TFT transfer plot of current vs. V_G for pentacene (p-type). Inset: I_{DS}-V_{DS} plot as a function of V_G (a = 0 – -3 V, b = -4 V, c = -5 V) showing forward (black) and reverse (red) V_{DS} scans. **c.** Current-voltage plot as a function of V_G for **CuFPc** (n-type). **d.** corresponding TFT transfer plot of current vs. V_G.
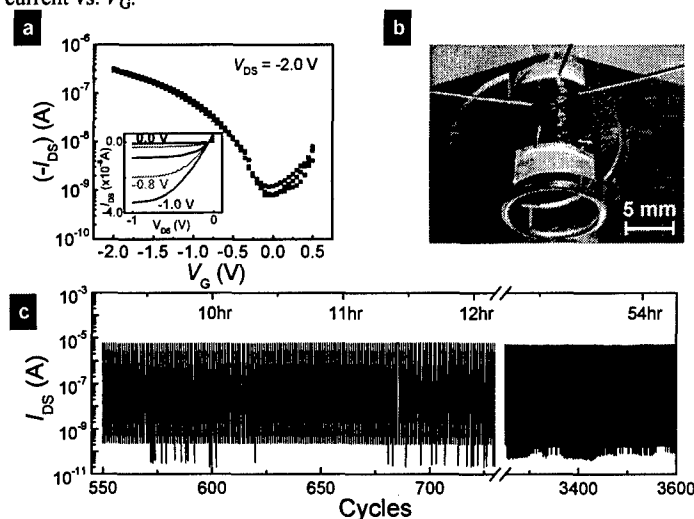
Figure 19. Performance of a pentacene TFT device having a **CPVP-C$_6$** gate dielectric. **a.** Transfer plot of current vs. V_G on an Al foil gate before bending (red), after bending 10 times (black), and after bending 30 times (blue). The measurements after bending were carried out on a bent device, with a curvature radius of 7 mm. Inset: Corresponding

23

current-voltage plot as a function of V_G. **b.** Image of the device on an Al foil gate during measurement. Scale-bar denotes 3 mm. **c.** OTFT operational stability in air driven by square-wave pulses V_G = 0 V to + 3V at 5 Hz (V_{DS} = +3 V).

In conclusion, we have demonstrated here that blending of appropriate commercially-available polymers and organosilane crosslinking agents affords robust, smooth, adherent, pinhole-free, high-capacitance, low-leakage ultra-thin (10-20 nm) gate dielectric materials. These films are readily deposited from solution, adhere strongly to a variety of rigid and flexible conducting substrates, can be patterned, and are compatible with a broad range of organic semiconductors. The resulting OTFTs function at unprecedentedly low operating voltages for a polymer-based gate dielectric. These results demonstrate that implementing these polymer dielectrics in solution-processing methodologies offers low voltage, low power operation.

4. Electrical Contact in n-channel oFETs

Before embarking on the Phase I project, the nature of the electrical contact in n-channel organic field effect transistors was not well understood (in comparison with p-channel field-effect transistors). In most reports in the literature, the quoted mobility values are for the so-called top-contact devices in which the source and drain electrodes are defined after the semiconductor is deposited. In many of these materials, the performance of bottom contact devices, in which the source and drain are first defined before the semiconductor is deposited, is much worse than that of top contact devices. Often, the mobility in the bottom contact configuration is many orders of magnitude lower than that of devices in the top contact configurations. The chief reason for this is that in the bottom contact configuration, the surface relief at the step where the source and drain electrodes are defined results in the growth of a disordered semiconductor region with a very low mobility and poor carrier transport properties. This problem is compounded by the fact that most metals are very hydrophilic and affect the molecular ordering and orientation of the organic semiconductor in proximity to the metal such that there is are barriers to facile transport. The reports on contacts to organic transistors in the literature were mainly on p-channel devices. Thus, there was a need to systematically study electrical contacts in n-channel OFETs. This was accomplished by The University of Texas group in Phase I.

We first studied contact injection in top contact DHFCO-4T transistors, which have the highest mobility among the n-channel organic thin-film transistors that any group have reported. In particular, we note that collaborators from Northwestern have obtained mobility values of 2 cm^2/V-s. We have designed shadow masks which result in channel lengths of 50 μm to 1 mm. The purpose of this study is to see if the extracted mobilities decrease with decreasing channel length. If they do than we have a problem with carrier injection. We used Au and Ag as the two metals and the results are similar and are summarized in Table I below for silver. The result indicates that there is no clear fall-of in mobility with decreasing channel length. This implies that both Au and Ag contacts function fairly well for this material. The

24

Mobility Summary

	Silver electrode (HMDS + Oxygen plasma)						
Width (µm)	500	800	1,000	5,000	10,000	10,000	10,000
Length (µm)	50	80	100	500	1,040	1,090	1,140
W / L	10	10	10	10	9.6	9.2	8.8
Saturation regime Mobility (cm²/Vs) (V_{DS} = 60 V)	0.29	0.33	0.38	0.41	0.32	0.29	0.26
I_{on} / I_{off} ratio (V_{DS} = 60 V) (V_g = 0~60 V)	5.1×10^3	3.5×10^3	3.6×10^3	1.1×10^3	7.6×10^2	7.2×10^2	7.7×10^2

We developed a method for detailed evaluation of the contact resistance of gold/DHFCO-4T contacts in devices with a channel length ~ 1 mm. The findings at that time were that the contact resistance is a small fraction of the total resistance that includes the channel resistance. The data shown above indicates that even in shorter channel length devices (for channel lengths as small as 50 µm), the effective mobility does not fall off significantly. This is an important prerequisite for fabricating circuits, where short channel lengths are desired for higher speed. The results are shown in Table II below

Mobility summary

|		No metal strip	1 metal strip	2 metal strip	3 metal strip
W / L (µm)		10,000 / 840	10,000 / 890	10,000 / 940	10,000 / 990
Mobility (cm²/Vs)	Linear regime (V_{DS} = 3 V)	0.31	0.27	0.23	0.21
	Saturation regime (V_{DS} = 35 V)	0.78	0.59	0.39	0.32
I_{on} / I_{off} (V_g = 0~35 V)		4.82×10^4	4.55×10^4	4.03×10^4	3.07×10^4

Table II: Effect of additional metal strips on the apparent mobility of DHFCO-4T transistors

For fabricating circuits, it is generally required to employ bottom contact structures in order to achieve small channel lengths. OrganicID is exploring alternative top-contact fabrication

25

approaches based on laser ablation and these will be discussed below after a description of the techniques and knowledge developed in modifying bottom contacts to achieve reasonable mobility values for two semiconductors: DHFO-4T and FTPCDI.

In the case of DHFCO-4T untreated Au results in bottom contact transistors that do not function well. The mobilities are extremely small. This is because of the disordered region between the semiconductor layer that grows on gold and the adjacent semiconductor layer that grows on SiO$_2$ (the gate insulator). After experimenting with several combinations of surface treatments to improve the electrical performance of such devices, we found that the sequential use of two self-assembled monolayers (SAMs) before depostition of the DHFCO-4T results in vastly improved performance. The two SAMs we employ are hexamethyl disilazane (HMDS) and nitrobenzene thiol. The HMDS is ampiphilic and bonds to the SiO$_2$ such that its hydrophobic tail is exposed to the surface. The sulfur in the nitrobenzene thiol bonds to the Au and creates a surface which is much more hydrophobic than Au. When the semiconductor is deposited after such treatments, the field-effect mobility is in excess of 10^{-2} cm^2/V-s. This value is still lower than that attained with top-contact geometry devices. It represents, however, a major improvement on bottom-contact mobilities without surface treatments.

Similar results were obtained for FPTCDI for bottom contact devices. The combination of HMDS and nitrobenzene thiol works fairly well in this case and small geometry devices (channel length of 4 mm) with mobilities in excess of 10^{-2} cm^2/V-s have been obtained.
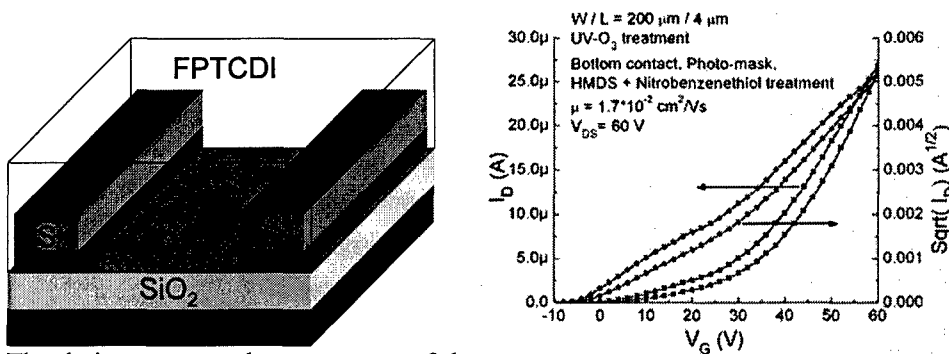
The drain current and square –root of the drain current as a function of gate voltage are shown above. The hysteresis is modest and the threshold voltages are not very large.

With the semiconductor, we obtained one of the highest bottom contact mobilities in short channel length devices (4 microns). The results are shown in the figure below. Mobility levels of 0.14 cm^2/V-s were achieved after treating the sample surface with a combination of treatments including an oxygen plasma, HMDS vapor and octadecanethiol. The on/off ratio is also very high.
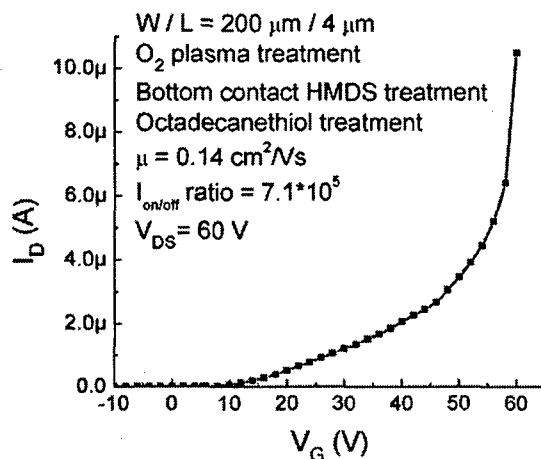
Yet another technique to improve electrical contact to n-channel OFETs was developed under Phase I. In this method a tunneling pn junction between PEDOT (a highly p-doped conducting polymer) and the field-induced electrons in the channel is used to facilitate injection. This is new method hitherto never used for n-channel OFETs. The results are very encouraging with mobilities of 0.18 cm^2/V-s second achieved. This suggests that in making electrical contact to bottom contact OFETs, it is more important to preserve the morphology of the semiconductor at and near the interface with the contacts than in optimizing work-function.

5. Inverter devices

Since we have developed new n-type semiconductors and dielectric materials fully compatible with both p- and n-type transport, complementary logic devices were also fabricated. The investigated inverters structures are reported in Table 1. A number of substrate-gate materials and p-/n-type semiconductors have been employed. The dielectric of choice is the ultra-thin crosslinked **CPVP-C6,** which should allow low-voltage invertor operation.

Table 1. Structure and inverter device characteristics.

Invertor #	Substrate/gate	p-type	n-type	dV_{OUT}/dV_{IN}
I-1	n^+-Si	pentacene	FPcCu	3.5
I-2	Al foil	pentacene	FPcCu	3.4
I-3	PEN/Al	pentacene	FPcCu	3.4
I-4	PEN/Al	pentacene	PDI-CN$_2$	In progress
I-5	PEN/Al	dH-PTTP	PDI-CN$_2$	In progress

27
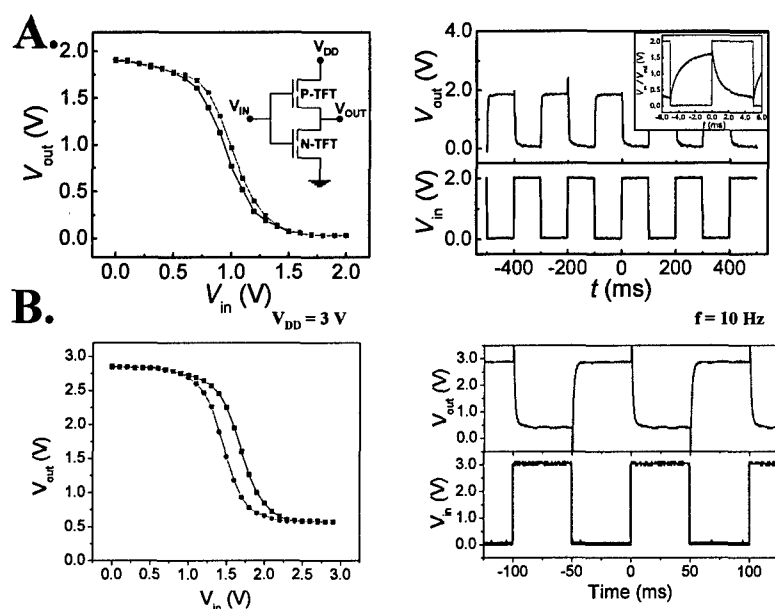
Figure 20. Complementary PVP-C_6 inverters using a pentacene TFT (L = 100 µm, W = 5000 µm) and a **CuFPc** TFT (L = 50 µm, W = 5000 µm) on n^+-Si (A) and PEN-Al (B) substrate gate. **Left.** Static characteristics measured with increasing (black) and decreasing (red) input voltage (V_{DD} = + 2 V). **Inset:** Schematic electrical connections of the inverter. **Right.** Dynamic switching characteristics of the inverter at 5 Hz. **Inset:** Dynamic switching characteristics of the inverter at 100 Hz.

All devices were fabricated with a common gate as input voltage (V_{IN}) and operate at very low voltages. Inverter response is clearly observed for switching between logic "1" (- 2/ - 3 V) and logic "0" (0 V) with the small hysteresis reflecting the transistor threshold voltage stability. The voltage gain $dV_{OUT}/dV_{IN} > 1$ implies that these devices could be used to switch subsequent stages in more complex logic circuits. These inverters can be switched at frequencies up to ~ 100 Hz, with a τ ~ 1 ms fall time and a τ ~ 1 ms rise time. Obvious improvements are expected by employing even higher-mobility n-type materials, patterning the gate electrode (to reduce source-drain-to-gate overlap capacitance), and reducing channel length (the channel length in these proof-of-concept devices is 100 µm, greater than 5-10 µm typically used in optimized organic ICs). Figure 20 shows static and dynamic responses for inverter I-1 and flexible inverter I-3.

6. Circuits

Tasks 5 and 6 require us to fabricate and characterize complementary inverters. We have described the characteristics of inverters in above. We have proceeded a step further and have fabricated some ring oscillator circuits with bottom-contact long channel length devices. This work is a prelude to more detailed circuit fabrication that is under way. We have obtained functioning complementary ring-oscillators with pentacene p-channel FETs and DHFCO-4T n-channel FETs. We emphasize that the channel lengths of devices in these circuits is large. With suitable scaling down, the speeds of ring oscillators will go up.
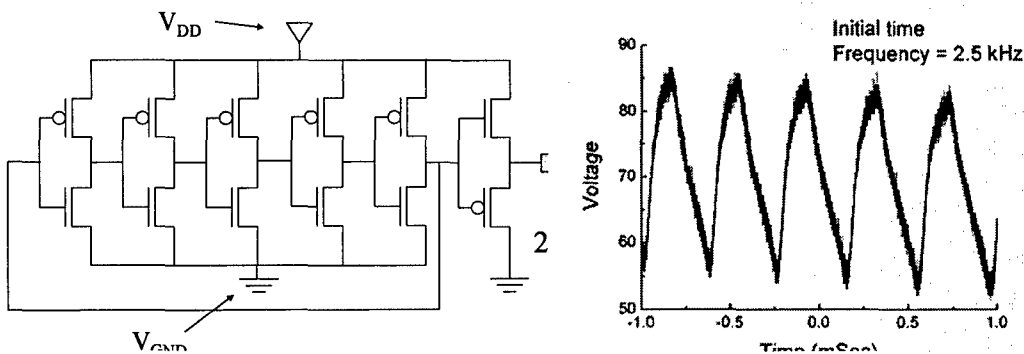
In phase I, the highest ring oscillator sped achieved was 10 kHz for a 5-stage ring oscillator with pentacene p-channel transistors and PDI-8CN$_2$ n-channel transistors. The channel length was near 8 microns and there was substantial overlap between gate and S/D metal levels resulting in high capacitance. Another possible route to increase the speed of ring oscillators is to use small geometry top-contact transistors, which tend to have a higher carrier mobility. OrganicID is experimenting with laser ablation of deposited metals such as Au to achieve the small geometries needed for high speed and the high mobilities characteristic of top-contact geometry devices. This approach will be explored in Phase II and will complement continued efforts to obtain bottom-contact mobilities that are similar to top-contact mobilities.

7. Experimental Procedure and Instruments

Synthesis. The organic semiconductors pentacene and copperphthalocyanine are commercially available. The other semiconductors have been synthesized according to the procedures reported previously by our group or described in reports 1-3. The synthesis of new compounds is described below.

(2,3,5,6-tetrafluorophenyl)(5-bromothien-2-yl)methanone. To a mixture of perfluorobenzoyl chloride (2.51 g, 10.9 mmol) and 2-bromothiophene (1.86 g, 11.4 mmol) in carbon disulfide (80 mL), aluminum chloride (2.90 g, 21.8 mmol) was added in portions over 10 min with vigorous mechanical stirring. The reaction turned red and was stirred for 2.5 h before being quenched with water (80 mL). The organics were separated, the aqueous layer extracted with carbon disulfide (3 x 50 mL), and the combined organics washed with water (3 x 100 mL) and dried over MgSO$_4$. The organics were concentrated in vacuo and the residue eluted through a silica gel column (hexane : ether = 9 : 1) to yield 1.23 g (32 %) green crystals. mp 123 °C; ^{1}H NMR (DMSO): δ 7.78 (d, 2H, ^{2}J=3.6 Hz), 7.54 (d, 2H, ^{2}J=4.4 Hz); ^{19}F NMR (DMSO): δ -142.1 (m, 2H), -151.6 (m, 1H), -160.6 (m, 2H) Anal. Calcd for C$_{11}$H$_2$BrF$_5$OS: C 37.00, H .056. Found: C 37.37, H 0.83; MS (EI): m/z (%) 355.8 (92) [M$^+$].

5,5'''-bis(perfluorophenylcarbonyl)-2,2':5',2'':5'',2'''-quaterthiophene **(DFCO-4T, 1).** A mixture of (2,3,5,6-tetrafluorophenyl)(5-bromothien-2-yl)methanone **(6)** (0.511 g, 1.43 mmol), 5,5'-bis(tributylstannyl)-2,2'-dithiophene (0.532 g, 7.15 mmol), and tetrakis(triphenylphosphine)palladium(0) (0.0250 g, 0.0215 mmol) was degassed with nitrogen three times before 8 mL anhydrous DMF was added. The reaction was heated to 80 °C for 10 h with stirring. A red-brown precipitate formed and upon cooling was collected by filtration, washed with hexanes (3 x 10 mL) and methanol (3 x 10 mL). Gradient sublimation (2x) afforded a bright orange crystalline material (0.305 g, 60 %) with some crystals suitable for x-ray diffraction. mp 312 °C; ^{1}H NMR (DMSO): δ 7.87 (d, 2H, ^{2}J=3.2 Hz), 7.70 (d, 2H, ^{2}J=3.2 Hz), 7.60 (d, 2H, ^{2}J=4.4 Hz), 7.54 (d, 2H, ^{2}J=4.0 Hz); ^{19}F NMR (DMSO): δ -142.3 (m), -152.0 (m), -160.7 (m); Anal. Calcd for C$_{30}$H$_8$F$_{10}$O$_2$S$_4$: C 50.14, H 1.12, F 26.11. Found: C 50.00, H 1.30, F 26.11; MS (EI): m/z (%) 717.8 (100) [M$^+$].

(5-bromothien-2-yl)(phenyl)methanone. To a mixture of benzoyl chloride (2.81 g, 20.0 mmol) and 2-bromothiophene (3.42 g, 21.0 mmol) in carbon disulfide (120 mL) aluminum chloride (5.34 g, 40.0 mmol), was added in portions over 10 min with vigorous magnetic stirring. The reaction was allowed to stir for 2.5 h before being quenched with 100 mL 1 M HCl(aq). The organics were separated, the aqueous layer extracted with carbon disulfide (3 x 50 mL), and the combined organics washed with water (3 x 100 mL) and dried over MgSO4. The organics were concentrated in vacuo and the residue eluted through a silica gel column (hexane : ether = 9 : 1) to yield 5.14 g (96 %) of yellow crystals. mp 141 °C (lit[1] 76 °C); ^{1}H NMR (CDCl3): δ 7.84 (d, 2H, ^{2}J=8.0 Hz), 7.62 (t, 1H, ^{3}J=7.2 Hz), 7.52 (t, 2H, ^{3}J=7.5 Hz), 7.40 (d, 2H, ^{2}J=3.5 Hz), 7.15 (d, 2H, ^{2}J=4.0 Hz).

5,5'''-bis(phenylcarbonyl)-2,2':5',2'':5'',2'''-quaterthiophene (DPCO-4T, 2). A mixture of 2-bromo-5-benzoylthiohene (1.07 g, 4.00 mmol), 5,5'-bis(tributylstannyl)-2,2'-dithiophene (1.49 g, 2.00 mmol), and tetrakis(triphenylphosphine)palladium(0) (0.0693 g, 0.0600 mmol) was degassed with nitrogen three times before 20 mL anhydrous DMF was added. The reaction was heated to 80 °C for 15 h with stirring. A deep red precipitate formed and upon cooling was collected by filtration, washed with hexanes (3 x 10 mL) and methanol (3 x 10 mL). Gradient sublimation (2x) afforded an orange-red crystalline material (0.689 g, 64 %) with some crystals suitable for x-ray diffraction. mp 303 °C; ^{1}H NMR (DMSO): δ 7.85 (2H), 7.84 (2H), 7.67 (4H), 7.59 (2H), 7.53 (2H), 7.48 (1H), 7.44 (1H); Anal. Calcd for $C_{30}H_{18}O_2S_4$: C 66.88, H 3.37. Found: C 66.93, H 3.42; MS (EI): m/z (%) 538.0 (100) [M$^+$].

P(COFCO-4T) (3). A mixture of 4,4'-dioctyl-5,5'-bis(tributylstannyl)-2,2'-dithiophene (0.969 g, 1.00 mmol), 1,4-bis((5-bromothien-2-yl)carbonyl)-2,3,5,6-tetrafluorobenzene (0.530 g, 1.00 mmol), and tetrakis(triphenylphosphine)palladium(0) (34.7 mg, 0.0300 mmol, 0.03 equiv.) was degassed with nitrogen three times before 10 mL anhydrous DMF was added. The reaction was heated to 110 °C for an additional 72 h during which time four equal amounts of tetrakis(triphenylphosphine)palladium(0) (34.7 mg, 0.0300 mmol, 0.03 equiv.) were added every 12 h. After cooling, a red precipitate was isolated by filtration through a 0.45 um filter, washed with methanol (200 mL). The powder was dissolved in CHCl3, precipitated with methanol, and centrifuged to give black pellets which became translucent red upon drying in a vacuum oven. This process was repeated three times to give 3 (342 mg) as translucent red flakes soluble in toluene, xylenes, trichlorobenzene, thiophene, and THF. This material had a MW of 15,300 by HT-GPC (140 °C, trichlorobenzene). ^{1}H NMR (CDCl3): □ 7.51 (m, 2H), 7.13 (s, 1H); ^{19}F NMR (CDCl3): □ -138.97 (s), -139.03 (s); ^{119}Sn NMR □ -4.2 (s); Anal. Calcd for $C_{40}H_{40}F_4O_2S_4$: C 63.46, H 5.33. Found: C 63.20, H 5.44.

Synthesis of NDI-8CN₂
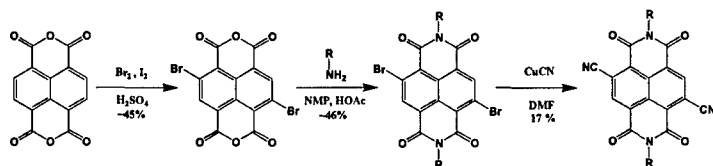
2,6-dibromonapthalene-1,4:5,8-tetracarboxylicdianhydride(1): To a 500 mL roundbottom was added 19.8g (73.8 mmol) of naphthalene 1,2:5,6- tetracarboxylic dianhydride and 100 mL of oleum. The suspension was stirred for 3 hours, followed by addition of 0.8124g (3.2 mmol) of I2. Stirring was continued for 1 more hour. To the reaction mixture, 8 mL (156 mmol) of Br2 were added drop-wise over 15 minutes. The reaction mixture was heated to 95 °C under N2 for 48

hours and then allowed to cool to room temperature. 300 mL of ice water was added to a 600 mL beaker, and the reaction mixture was slowly poured into the ice water. The yellow precipitate was filtered, washed 3 x 15 mL with MeOH, and dried to yield 24.1 g of crude product. Attempts at recrystallization failed, and the product was used crude for subsequent steps. The yield is estimated at ~45% based on MALDI-TOF-MS intensities. Maldi-TOF-MS: 426.91 (calcd 425.97)

N,N'-bis(n-octyl)-2,6-dibromonapthalene-1,4:5,8-tetracarboxylicdiimide(2)[1]: To a 250 mL roundbottom flask was added 2.1748g (5.106 mmol) of **1**, 100 mL of N-methyl pyrollidinone, 50 mL of glacial acetic acid, and 8.2 mL(81 mmol) of n-octylamine. The reaction was stirred at 85°C under N_2 for 6 hours. After cooling to room temperature, the reaction mixture was poured into 250 mL of MeOH and put in a –10°C freezer overnight. The precipitate was filtered, washed 3x15mL with MeOH and dried. The crude orange product was columned in dichloromethane, and the second spot collected to give 1.5084g (2.326mmol, 46% yield) of yellow product. ^{1}H NMR (CDCl$_3$): δ 8.997 (s, J = 8.15 Hz, 2H), δ 4.189 (m, 4H). Maldi-TOF-MS: 648.77 (calcd 648.43).

N,N'-bis(n-octyl)-2,6-dicyanonapthalene-1,4:5,8-tetracarboxylicdiimide(NDI-8CN$_2$): To a 500 mL roundbottom flask was added 2.14 g(23.9 mmol) of CuCN, 1.4501g (2.236mmol) of **2**, and 100 mL of dimethylformamide. The reaction mixture was stirred under N_2 for 5 hours at 140 °C. After the reaction mixture was cooled, the solvent was removed on a rotoevaporator. The crude product was dissolved in chloroform, filtered, and the precipitate was thoroughly washed with chloroform. The filtrate was rotovapped to dryness, and the resulting solid was columned in dichloromethane to yield 205mg (0.379 mmol, 17% yield) of NDI-8CN$_2$. Maldi-TOF-MS: 541.06 (calcd 540.65)

Synthesis of poly((3,4-N-n-alkyl-imido)thiophene) – Ullmann coupling route
3,4-dicyanothiophene (1). A stirred suspension of 3,4-dibromothiophene (24.2 g, 0.1 mol) and copper(I) cyanide (26.0g, 0.29 mol) in dry DMF (25 mL) was refluxed under N_2 for 4 hr. The dark mixture was poured into a solution of hydrated ferric chloride (100 g) in hydrochloric acid (175 mL, 1.7 M) and maintained at 60-70°C for 1 hr. The mixture was let to cool down to room temperature, and methylene chloride (125 mL) was added and the layers were separated. The aqueous phase was extracted four times with 125 mL portions of methylene chloride. Organic phase was combined and was washed successively with two 100 mL portions of hydrochloric acid (6 M), water, saturated sodium bicarbonate solution, and finally with distilled water, followed by drying over MgSO$_4$ over night. Solvent was evaporated to dryness to afford a pale yellow solid. Recrystallization from acetonitrile provided a white crystal (12.0 g, 90%). ^{1}H NMR (CDCl$_3$) δ 8.0; ^{13}C NMR (CDCl$_3$) δ 136.8, 113.1, 111.8.
Thiophene-3,4-dicarboxylic acid (2). A suspension of **1** (9.2 g, 68.6 mmol) in 100 mL concentrated HCl was refluxed for 6 hrs. Heating was removed and colorless crystal formed was collected via vacuum filtration. Recrystalization from water afforded a colorless crystal (9.85 g, 83%). ^{1}H NMR (CDCl$_3$+DMSO-d$_6$) δ 8.10; ^{13}C NMR (CDCl$_3$+DMSO-d$_6$) δ 164.0, 136.5, 131.0.
2,5-dibromo-thiophene-3,4-dicarboxylic acid (3). To **2** (1.0 g, 5.8 mmol) in 10 mL glacial acetic acid was added bromine (1.8 mL, 35 mmol) dropwise. The mixture was stirred over night and a colorless crystal was formed. The bromine was removed by adding saturated NaHSO$_3$ solution, and the precipitate was collected by filtration. Recrystalization from water followed by drying gives a colorless crystal (1.2 g, 63%). ^{13}C NMR (CDCl$_3$) δ 163.1, 134.6, 114.7.
2,5-dibromothiophene-3,4-dicarboxylic acid dichloride (4). To **3** (1.0 g, 3.03 mmol) in 5 mL anhydrous benzene was added oxalyl chloride (1.1 mL, 12.2 mmol) and one drop of dry DMF. The mixture was heated to reflux for 1 hr, and allowed to cool to room temperature. The volatiles were removed in vacuo to afford **4** (1.0 g, 90%).

3,4-N-(n-octylimido)-2,5-dibromothiophene (5a). 4 (1.0 g, 2.7 mmol) was mixed with n-octylamine (0.45 mL, 2.7 mmol) in a reaction tube and heated to 140°C for 30 min under vigorous stirring. The preparation was cooled to room temperature and chromtographed over silica gel with CH_2Cl_2:hexane (10:1) to afford a white powder (0.35 g, 31%). ^1H NMR ($CDCl_3$) δ3.59 (2H), 1.63 (2H), 1.30 (10H), 0.88 (3H); ^{13}C NMR ($CDCl_3$) δ 160.6, 135.0, 113.1, 39.0, 32.0, 29.3, 28.4, 27.0, 22.8, 14.3.

3,4-N-(n-dodecylimido)-2,5-dibromothiophene (5b). 4 (1.0 g, 2.7 mmol) was mixed with n-dodecylamine (0.5 g, 2.7 mmol) in a reaction tube and heated to 140°C for 30 min under vigorous stirring. The preparation was cooled to room temperature and chromtographed over silica gel with CH_2Cl_2:hexane (10:1) to afford a white powder (0.45 g, 50%). ^1H NMR ($CDCl_3$) δ3.55 (2H), 1.60 (2H), 1.20 (18H), 0.83 (3H); ^{13}C NMR ($CDCl_3$) δ 160.8, 134.9, 113.1, 38.7, 32.2, 29.8, 29.78, 29.7, 29.5, 29.4, 28.7, 27.1, 22.8, 14.3.

3,4-N-(2',2',3',3',4',4',4'-heptafluorobutyl)-imido) -2,5-dibromothiophene (5c). 4 (1.0 g, 2.7 mmol) was mixed with 2,2,3,3,4,4,4-heptafluorobutyl amine (0.4 mL, 2.7 mmol) in a reaction tube and heated to 140°C for 30 min. The preparation was cooled to room temperature and chromtographed over silica gel with CH_2Cl_2:hexane (15:1) to afford a white powder (0.45 g, 34%). ^1H NMR ($CDCl_3$) δ4.30 (2H); ^{13}C NMR ($CDCl_3$) δ159.07, 134.05, 115.18, 37.85.

Ullmann Polymerization

A typical procedure involved mixing 5 (0.2 g, 0.47 mmol) and freshly activated Cu powder (0.12 g, 1.85 mmol) in 2.0 mL dry DMF and heated the mixture to 150°C for two days under N_2. The content was allowed to cool and poured into 100 mL $CHCl_3$. Cu powder was removed by filtration and the filtrate was poured into CH_3OH (200 mL). The mixture was allowed to stand over night. Vacuum filtration yielded a black powder. The powder was extracted in a Soxhlet extractor with methanol for one day, followed by hexane extraction one day, and was thoroughly extracted with chloroform. The polymer was precipitated with methanol (200 mL) and dried under high vacuum (87 mg, 69%).

Anal.: poly((3,4-N-n-octylimido)thiophene) (**PC8I**), calcd for $(C_{14}H_{17}NO_2S)_n$: C 63.58, H 6.51, N 5.32, found C 63.33, H 6.59, N 5.12.

poly((3,4-N-n-dodecylimido)thiophene) (**PC12I**), calcd for $(C_{18}H_{25}NO_2S)_n$: C 67.67, H 7.89, N 4.38, found C 67.32, H 7.92, N 4.36.

Synthesis of (3,4-N-n-alkyl-imido)thiophene-thiophene coplymer – Stille coupling route

Synthesis of PC8ITT. A mixture of **5a** (200 mg, 0.47 mmol) and 2,5'-di(tri-n-butylstannyl)bithiophene (357 mg, 0.47 mmol)was dissolved in dry DMF (2 mL) in a 10 mL Schelnk line flask. To the solution was added CsF (143 mg, 0.94 mmol, 200%). Pd(PPh_3)_4 (27 mg, 0.024 mmol, 5%) and CuI (9 mg, 0.047 mmol, 10%) were added and the flask was evacuated and refilled with N_2 five times. The mixture was stirred at 60°C overnight, and diluted with $CHCl_3$ (50 mL) and water (20 mL). After vigorous shaking the organic layer was separated and passed through celite, dried over $MgSO_4$. $CHCl_3$ was concentrated to about 10 mL, and was poured into 200 mL methanol. The solid was collected by filtration, transferred to a Soxhlet thimble, and extracted successively with methanol (1 day), hexanes (1 day), and chloroform (1 day). The chloroform solution was concentrated to 10 mL, and was poured into 200 mL CH_3OH. The suspension was allowed to stand overnight in fridge, and the black precipitate was collected via vacuum filtration. The metallic solid was dried under high vacuum for one day. Yield: 110 mg (68%).

Synthesis of PC8IT. A mixture of **5a** (206 mg, 0.48 mmol) and 2,5-di(tri-n-butylstannyl)thiophene (314 mg, 0.48 mmol)was dissolved in dry DMF (2 mL) in a 10 mL Schelnk line flask. To the solution was added CsF (143 mg, 0.94 mmol, 200%). Pd(PPh_3)_4 (27 mg, 0.024 mmol, 5%) and CuI (9 mg, 0.047 mmol, 10%) were added and the flask was evacuated and refilled with N_2 five times. The mixture was stirred at 60°C overnight, and diluted with

CHCl$_3$ (50 mL) and water (20 mL). After vigorous shaking the organic layer was separated and passed through celite, dried over MgSO$_4$. CHCl$_3$ was concentrated to about 10 mL, and was poured into 200 mL methanol. The solid was collected by filtration, transferred to a Soxhlet thimble, and extracted successively with methanol (1 day), hexanes (1 day), and chloroform (1 day). The chloroform solution was concentrated to 10 mL, and was poured into 200 mL CH$_3$OH. The suspension was allowed to stand overnight in fridge, and the black precipitate was collected via vacuum filtration. The metallic solid was dried under high vacuum for one day. Yield: 67 mg (70%).

Synthesis of PC12IT. A mixture of **5b** (204 mg, 0.42 mmol) and 2,5-di(tri-n-butylstannyl)thiophene (274 mg, 0.42 mmol)was dissolved in dry DMF (2 mL) in a 10 mL Schelnk line flask. To the solution was added CsF (127 mg, 0.84 mmol, 200%). Pd(PPh$_3$)$_4$ (24 mg, 0.021 mmol, 5%) and CuI (8 mg, 0.042 mmol, 10%) were added and the flask was evacuated and refilled with N$_2$ five times. The mixture was stirred at 60°C overnight, and diluted with CHCl$_3$ (50 mL) and water (20 mL). After vigorous shaking the organic layer was separated and passed through celite, dried over MgSO$_4$. CHCl$_3$ was concentrated to about 10 mL, and was poured into 200 mL methanol. The solid was collected by filtration, transferred to a Soxhlet thimble, and extracted successively with methanol (1 day), hexanes (1 day), and chloroform (1 day). The chloroform solution was concentrated to 10 mL, and was poured into 200 mL CH$_3$OH. The suspension was allowed to stand overnight in fridge, and the black precipitate was collected via vacuum filtration. The metallic solid was dried under high vacuum for one day. Yield: 65 mg (63%).

Anal.: poly((3,4-N-n-octylimido)thiophene-co-thiophene) (**PC8IT**), calcd for (C$_{18}$H$_{19}$NO$_2$S$_2$)$_n$: C 62.58, H 5.54, N 4.05, found C 56.41, H 5.93, N 3.06.

poly((3,4-N-n-dodecylimido)thiophene-co-thiophene) (**PC12IT**), calcd for (C$_{22}$H$_{27}$NO$_2$S$_2$)$_n$: C 65.8, H 6.78, N 3.49, found C 58.69, H 5.47, N 3.79.

Materials. n$^+$-Si wafers (Montco Silicon Tech) and ITO-coated glass substrates (≤30 Ω/sq, Thin Film Devices) were cleaned according to standard procedures. Aluminum substrates were cut from commercially available Al foil (Reynolds Customer Products).

Physical Measurements. ^{1}H and ^{19}F NMR (400 MHz) spectra were measured in CDCl$_3$, CD$_2$Cl$_4$, or toluene-d_8 with a Varian Mercury400 (room temperature) or a Varian Inova400 (variable temperature) instrument. Reported chemical shifts are referenced to solvent peaks. Optical absorption and emission spectra were obtained on THF solutions and as vacuum-deposited films (50 nm) with a Cary 1 Ultraviolet/Visible Spectrometer and a PTI QM2 Fluorescence Instrument (1 nm resolution), respectively. IR spectra were recorded on solid samples embedded in pressed KBr pellets using a Bio-Rad FTS-60. The mean of 32 scans, with 2 cm^{-1} resolution, were accumulated in all experiments. Thermal analysis was performed with a TA Instruments DSC 2920 Differential Scanning Calorimeter (N$_2$) and a TA Instruments SDT 2960 simultaneous DTA-TGA instrument (10^{-2} Torr N$_2$) at ramp rates of 10°C / min (DSC) and 1.5 °C / min (TGA). Cyclic voltammetry experiments was conducted using an Epsilon single-channel potentiometer and a BAS C3 cell stand: a one-compartment cell with a C disk working, bare Ag reference, and Pt wire counter electrodes. Appropriate precautions were taken to eliminate water and oxygen from the n-Bu$_4$NPF$_6$ / THF electrolyte medium.

Single Crystal X-Ray Diffraction Studies. Single crystals were grown from trichlorobenzene / tetrachloroethane solutions by slow cooling from approximately 120°C to 50°C or via slow vacuum sublimation. X-ray data were collected on a CCD area detector with graphite monochromated Mo-Kα radiation. Reflection data were collected with a Bruker SMART detector, processed with Saint-NT software (Bruker), and corrected for Lorentz and polarization effects. The structures were solved by direct methods and expanded using Fourier techniques. Non-hydrogen atoms were refined anisotropically, and hydrogen atoms were included but not refined.

Computational Details. All calculations were performed using density functional theory (B3LYP hybrid functional and the 6-31G* basis) using the Q-Chem program, version 2.0.2. Full geometry optimizations were performed for all molecules, starting with a flat interplanar conformation of the oligothiophene units and planar conformations of the carbon atoms in the alkyl or perfluoroalkyl chains. The lowest energy conformer was used for electronic structure analysis with no explicit adjustments for intermolecular packing effects.

X-Ray Diffraction Studies. Powder patterns were simulated from single crystal data using TEXSAN for Windows (version 1.0) or the Platon program.

Thin Film Growth. Prime grade n-doped silicon wafers (100) having 300 nm thermally grown oxide (Process Specialties) were used as device substrates. They were rinsed with water, methanol, and acetone before film deposition. Trimethylsilyl functionalization of the Si/SiO_2 surface was carried out by exposing the silicon wafers to hexamethyldisilazane (HMDS) vapor at room temperature in a closed container under nitrogen overnight. Organic compounds were deposited by either vacuum evaporation (pressures $< 10^{-5}$ Torr) at a growth rate of 0.3-0.5 Ås^{-1}, or by casting from xylenes solutions (concentrations 200 - 400 ppm, 10^{-4} - 10^{-2} M). Evaporated films were 500 Å thick (as determined by a calibrated in situ quartz crystal monitor), and solution-cast films were variable and thicker, on the order of microns. For solution depositions, a region of the substrate surface ($\sim$1-2 cm^2) was defined using 3M Novec™ EGC-1700 electronic coating (comparable to the previously used 3M FC-722 product) before casting.[21] The room temperature or warm solution was transfered inside the defined area and allowed to evaporate, with no special care taken to avoid dust in the environment (a clean hood is optional). For FET device fabrication, top-contact electrodes (500 Å) were deposited by evaporating gold (pressure $< 10^{-5}$ Torr); channel dimensions were 100/200 μm (L) by 4.0 mm (W). Annealing of films was carried out under N_2 for 10 min at a temperature $\sim$ 30 °C below the capillary melting point of the compound.

Thin Film Characterization. Thin films (500 Å) were analyzed by X-ray film diffractometry (XRD), using standard θ - 2θ techniques, with Cu Kα radiation and a monochromator. All θ - 2θ scans were calibrated with the reflection of the Si (100) substrates. Films were coated with 3 nm of sputtered Au before analysis by scanning electron microscopy (SEM) using a Hitachi S4500 FE microscope. Electrical measurements were performed using a home-built coaxial probe station and a Hewlett-Packard 4155A Semiconductor Parametric Analyzer. The capacitance of the insulator is 2 x 10^{-8} F/cm^2 for 300 nm SiO_2. A digital capacitance meter (Model 3000, GLK Instruments) and impedance/gain-phase analyzer (SI 1260, Solartron Analytical) were used for capacitance measurements.

8. Published work.

1. Facchetti, A.; Yoon, M.-H.; Yan, H.; Marks, T. J.
   "Low-Voltage Organic Field-Effect Transistors with Ultra-Thin Crosslinked Polymers as Gate Dielectrics"
   J. Am. Chem. Soc. **2005**, *in press.*

2. Facchetti, A.; Yoon, M.-H.; Marks, T. J.
   "Gate Dielectrics for Organic Field-Effect Transistors. New Opportunities for Organic Electronics"
   Adv. Mater, **2005**, *in press.*

3. Letizia, J.; Facchetti, A.; Ratner, M. A.; Stern, C. R.; Marks, T. J.
"High Electron Mobility in Solution Cast and Vapor Deposited Phenyl-Acyl-Quaterthiophene
Based Field-Effect Transistors: Toward N-Type Polythiophenes"
Manuscript submitted.

4. Yoon, M.-H.; Facchetti, A.; Marks, T. J.
"Exceptionally High n-Channel Mobility Enabled by a Double Layer Organic-Inorganic
Dielectric"
Manuscript in preparation

5. Yoo, B.; Facchetti, A.; Mohapatra, S.; Dimmler, K.; Marks, T. J.; Dodabalapur, A.
"Characterization and Improvement of Electrical Contacts to Novel n-Channel Organic
Transistors"
Manuscript in preparation

REPORT DOCUMENTATION PAGE

AFRL-SR-AR-TR-05-

0232

Public reporting burden for this collection of information is estimated to average 1 hour per response, including the time for reviewing instructions, searching existing dat
the collection of information. Send comments regarding this burden estimate or any other aspect of this collection of information, including suggestions for reduci
Operations and Reports, 1215 Jefferson Davis Highway, Suite 1204, Arlington, VA 22202-4302, and to the Office of Management and Budget, Paperwork Reduction F.

1. AGENCY USE ONLY *(Leave blank)*	2. REPORT DATE 14 Jun 05	3. REPORT TYPE AND DATES COVERED FINAL - from 01 Sept 04 to 31 May 05

4. TITLE AND SUBTITLE (STTR PHASE I) Organic Based Flexible Transistors and Electronic Devices	5. FUNDING NUMBERS FA9550-04-C-0080

6. AUTHOR(S)
Dimmler, Klaus

7. PERFORMING ORGANIZATION NAME(S) AND ADDRESS(ES) OrganicID, Inc. 495 Vanderbilt Court Colorado Springs, CO 80906	8. PERFORMING ORGANIZATION REPORT NUMBER

9. SPONSORING/MONITORING AGENCY NAME(S) AND ADDRESS(ES) AFOSR/NL 875 North Randolph Street Suite 325, Rm 22203 Arlington, VA	10. SPONSORING/MONITORING AGENCY REPORT NUMBER

11. SUPPLEMENTARY NOTES

12a. DISTRIBUTION AVAILABILITY STATEMENT Approve for Public Release: Distribution Unlimited	12b. DISTRIBUTION CODE

13. ABSTRACT *(Maximum 200 words)*

The Phase I materials development effort was highly productive with the proposed Phase I milestones accomplished or exceeded. The results of Phase I have successfully demonstrated that an air-stable, high mobility n-type organic material can be synthesized and integrated into a process to form an organic CMOS process. Phase I has further demonstrated effective solutions to the challenges that are generally associated with such integration, including the development of an appropriate dielectric and electrode which are compatible with p-type materials as well.

14. SUBJECT TERMS			15. NUMBER OF PAGES 35
			16. PRICE CODE

17. SECURITY CLASSIFICATION OF REPORT	18. SECURITY CLASSIFICATION OF THIS PAGE	19. SECURITY CLASSIFICATION OF ABSTRACT	20. LIMITATION OF ABSTRACT

Standard Form 298 (Rev. 2-89) (EG)
Prescribed by ANSI Std. 239.18
Designed using Perform Pro, WHS/DIOR, Oct 94

6-21-05